THESIS FOR THE DEGREE OF DOCTOR OF PHILOSOPHY

Exploring the nonlinear rheological behavior and optical properties of cellulose nanocrystal suspensions

Sylwia Wojno

Department of Industrial and Materials Science
Chalmers University of Technology
Gothenburg, Sweden, 2023

Exploring the nonlinear rheological behavior and optical properties of cellulose nanocrystal suspensions

Sylwia Wojno

ISBN 978-91-7905-881-4

ISSN 0346-718X
Ny serie 5347
This thesis has been prepared using LaTeX.

Department of Industrial and Materials Science
Chalmers University of Technology
SE-412 96 Gothenburg, Sweden
Phone: +46 (0)31 772 1000
www.chalmers.se

Cover image: "Cosmic CNCs" - micrograph from POM representing droplets of CNC^D exhibiting birefringent properties.

Printed by Chalmers Reproservice
Gothenburg, Sweden, August 2023

A scientist in his laboratory is not a mere technician: he is also a child confronting natural phenomena that impress him as though they were fairy tales.

Maria Skłodowska - Curie

Abstract

Cellulose nanocrystals (CNCs), with their versatile properties, offer immense potential in a range of applications, whether used independently or as sustainable reinforcements in polymers. They also find utility as renewable rheology modifiers in industries such as cosmetics, paints, and foods, where precise control over rheological characteristics is crucial for factors like product stability, prevention of splattering, and efficient processing and transportation. To enhance their properties and unlock new applications, surface modification of CNCs is essential. However, studying flow-induced structuring requires the use of accurate and reliable analysis methods, particularly when dealing with fast and large deformations in suspensions, multiphase systems, and composites.

This thesis presents a novel approach for studying the interactions between flow fields and CNCs by investigating nonlinear rheological parameters using a combination of Fourier-Transform rheology (i) and Polarized Light Imaging (PLI) techniques (ii). The utilization of (i) allows for the capture of nonlinear parameters that cannot be obtained through conventional rheological characterization. Concurrently, (ii) provides visual insights into flow-induced CNC structuring and optical properties.

By employing these two distinct techniques, it becomes possible to discern alterations in the microstructure of CNCs, enabling the determination of critical concentrations for phase transitions, percolation, and gelation.

To validate the proposed methodology, several different CNC systems were examined, categorized as either (1) self-assembling or (2) non-self-assembling CNC suspensions. These systems varied in terms of surface charge, concentrations, surface modification with azetidinium salts or monovalent counterions, and aspect ratio.

This comprehensive investigation expands our understanding of CNC behavior under flow conditions and offers valuable insights into the rheological properties of CNC suspensions, potentially paving the way for the development of improved materials and applications in various industries.

Keywords: Cellulose nanocrystals, nonlinear oscillatory shear, rheology, FT-Rheology, rheo-PLI, self-assembly.

Nomenclature

Roman Symbols

$2R$:	The diameter of parallel - plate geometry [mm]
G:	Shear modulus [Pa]
G':	(shear) Storage modulus [Pa]
G'_L:	Intra-cycle largest-strain secant modulus [-]
G'_M:	Intra-cycle minimum-strain modulus [-]
G":	(shear) Loss modulus [Pa]
$I(\omega)$:	Intensity spectrum [-]
$I_{3/1}$:	Third relative higher harmonic [-]
M:	Molar concentration [mol/L]
S:	Strain-stiffening parameter [-]
T:	Shear-thickening parameter [-]
t:	Time [s]

Greek Symbols

γ:	Shear strain [-]
γ_0:	(Shear) Strain amplitude [%]
$\dot{\gamma}$:	Shear rate [s^{-1}]
δ:	Phase angle [rad]
ζ:	Zeta-potential [mV]

η:	Shear viscosity [Pa·s]
η'_L:	Intra-cycle largest-strain secant dynamic viscosity [Pa·s]
η'_M:	Intra-cycle minimum-strain dynamic viscosity [Pa·s]
σ:	Shear stress [Pa]
ϕ:	Particle concentration
ϕ_c:	Percolation threshold
ϕ_g:	Gelation threshold
ω:	Angular frequency [rad/s]

Abbreviations

AFM:	Atomic Force Microscopy
ATR:	Attenuated Total Reflectance
BP:	Biphasic
$CDCL_3$:	Chloroform-D
CNC:	Cellulose nanocrystal
CNC_D:	Desulfated cellulose nanocrystal
DI:	Deionized water
DLS:	Dynamic Light Scaterring
DMSO:	Dimethyl sulfoxide
FT:	Fourier-Transform
FTIR:	Fourier-Transform Infrared
I-CNC:	Initial rod cellulose nanocrystal
IPA:	Isopropylic Alcohol

LAOS:	Large Amplitude Oscillatory Shear
LB:	Lissajous-Bowditch
LC:	Liquid crystalline
LR-CNC:	Long rod cellulose nanocrystal
LVR:	Linear viscoelastic regime
MCC:	Microcrystalline Cellulose
MAOS:	Medium Amplitude Oscillatory Shear
MCR:	Modular Compact Rheometer
NLVR:	Nonlinear viscoelastic regime
pCNC:	Pristine cellulose nanocrystal
PLI:	Polarized Light Imaging
POM:	Polarized Optical Microscopy
SAOS:	Small Amplitude Oscillatory Shear
SEM:	Scanning electron microscopy
SR-CNC:	Short rod cellulose nanocrystal
TEM:	Transmission electron microscopy
uCNC:	Untreated cellulose nanocrystal
qBP:	Quazi biphasic
WSO:	Weak strain overshoot
wt:	Weight percentage [%]

Contents

CHAPTER 1

Introduction

The demand for environmentally friendly and renewable resources has increased in the last decades, and wood has emerged as a viable option. Wood is composed of polymeric cellulose, hemicellulose, and lignin. Its hierarchical structure contains distinct elements at various length scales, ranging from the meter scale of the whole tree to the tens of nanometers of the molecular structures and chemical interactions of cellulose, hemicellulose, and lignin. The cellulose in wood is characterized by crystalline domains and exceptional strength due to its linear chain structure, and it can be modified for various industrial applications[1]. Cellulose nanoparticles can be extracted through chemical treatment or bleaching of wood fibers. Conversely, lignin has aromatic polymer units that form crosslinked three-dimensional structures and connect to the cellulose fibrils through hemicelluloses[2].

Despite the potential of CNCs, their application faces several challenges. The presence of hydroxyl groups makes them prone to self-association, leading to aggregation that can shield the active groups and reactive sites[3]. The aggregation of CNCs in suspensions is undesirable for their use as rheological modifiers in cosmetics, adhesives, and paints. Moreover, the hydroxyl groups reduce the performance of CNC-based films and coatings in terms of water

transmission[4]. The quality of optically active films also depends on the degree of helix orientation and the pitch length of CNC arrangements[5]. To overcome these challenges, the surface chemistry of cellulose nanoparticles can be modified. Additionally, functionalization with different salts can enhance the unique properties of CNC particles.

Therefore, it is necessary to employ specialized methods to comprehend the fundamental inter-particle interactions in cellulose-based products under simple shear and extensional conditions to obtain desirable properties. Rheological measurements have been employed to characterize various forms of cellulose for many applications, such as drug delivery and personal care products. However, most studies have focused on steady shear tests.

To investigate dispersion microstructure, dynamic behavior, and phase transitions, it is essential to understand inter-particle interactions. State-of-the-art rheological characterization techniques, which focus on nonlinear material response functions, can help to investigate features that are not observable in linear viscoelastic measurements. However, since these techniques are relatively new, there is a strong need to explore the significance of nonlinear material parameters, especially for systems relevant to materials science.

The present thesis explored the nonlinear rheological techniques such as Fourier Transform Rheology (FT Rheology) and stress decomposition to analyze microstructure changes in cellulose nanocrystal (CNC) based systems. The focus was on exploring the potential of new nonlinear material parameters to understand inter-particle interactions. The results were complemented with Rheo-PLI, a technique that can detect birefringence and phase transitions, to evaluate the suitability of the CNC-based systems for optical applications. Additional other techniques characterizing the structure and morphology of CNCs were performed.

1.1 Background of research project

This thesis is a part of Wallenberg Wood Science Center's (WWSC) Program 5, which is dedicated to exploring new materials derived from trees. WWSC has been researching wood-based materials for over a decade, intending to generate knowledge and expertise for developing environmentally-friendly materials. Even though CNC particles have been known for over 60 years, there is still a lack of clear understanding regarding the phase transitions and viscosity

behavior of CNC suspensions. Depending on many factors, such as aspect ratio, sulfate content, concentration, these suspensions have the ability to align themselves along the direction of flow under shear, and exhibit birefringence properties or not, while increasing viscosity. Consequently, the primary scientific objective of this thesis was to thoroughly investigate and understand the alterations occurring in the microstructure and inter-particle interactions within CNC suspensions. This exploration was primarily achieved through the utilization of several rheological characterization techniques.

1.2 Outline of thesis

In Chapter 2 of this thesis, a concise overview of cellulose is presented, followed by an introduction to various modifications of CNCs. Furthermore, the chapter delves into the grafting of azetidinium salts onto the surface of CNCs and briefly explains CNCs inherent tendency for self-assembly. As a result of this self-assembly, intriguing optical properties emerge. The subsequent chapter, Chapter 3, focuses on the materials employed in preparing the suspensions, providing an in-depth analysis of the preparation process.

Chapter 4 of this thesis provides a comprehensive account of the characterization methods employed in this study. It encompasses a range of techniques utilized to analyze the morphology of CNCs, including DLS (Dynamic Light Scattering), NMR (Nuclear Magnetic Resonance), TEM (Transmission Electron Microscopy), and POM (Polarized Optical Microscopy). The chapter also introduces the concepts of viscoelasticity and linear and nonlinear rheology, elucidating the principles behind Small Amplitude Oscillatory Shear (SAOS) and Large Amplitude Oscillatory Shear (LAOS). Furthermore, it briefly outlines the application of Fourier-Transform Rheology (FT-R) and the derivation of nonlinear parameters from these measurements.

Chapter 5 summarises the results of the performed measurements, and the influence of various factors such as concentration, ionic strength, modification type and phase transitions in CNC is discussed.

Finally, Chapter 6 provides the study's conclusions and discusses current and future work.

CHAPTER 2

Cellulose

Cellulose is a highly abundant natural polymer found in plants, algae, and certain bacteria, known for its structural strength and rigidity. It serves as a fundamental building block in the cell walls of plants, providing stability and support to their structure[6], [7]. Its production exceeds 10^{11} tons annually [8], and it has been utilized for centuries in various ways. Anselme Payen was the first one who successfully isolated cellulose from plant matter and few years later Herman Staudinger successfully determined its chemical structure[9], [10]. The term "cellulose" originates from a combination of french and latin. It is derived from the French word "cellule," meaning "small cell," and the latin suffix "-ose," denoting a sugar or carbohydrate. This name reflects the abundance of cellulose in the form of small cell-like structures found in plants and other organisms where it is prevalent. In Sweden, where forests cover 64% of the land[11], there is considerable interest in cellulose and wood-based compounds. While paper and textile products are the most well-known uses of cellulose, its versatility and possibility of surface modification has led to its application in new areas[12]–[14].

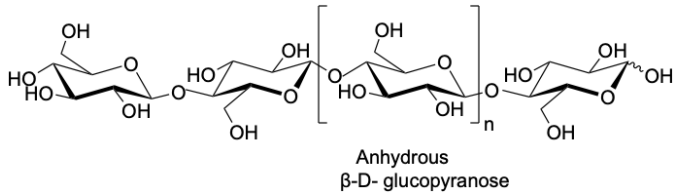

Figure 2.1: The molecular structure of cellulose.

2.1 The structure of cellulose

Cellulose is a biopolymer consisting of elongated, linear chains of β-D-glucose units. The glucose molecules within the cellulose chain are linked by a single oxygen atom, connecting C-1 of one ring to C-4 of the next ring (as depicted in Fig. 2.1). These glucose units, called anhydroglucose units, undergo dehydration reactions to form acetals, resulting in the loss of a water molecule [15]. Cellulose possesses favorable fiber-forming properties due to the equatorial orientation of hydroxyl groups and the β configuration of the C-1 oxygen. The cellulose polymers aggregates into layered sheets of cellulose polymers that stack on top of each other and imparts specific imparts specific characteristics like hydrophilicity, chirality, resistance to aqueous solvents, and non-melting behavior[16]. Native cellulose exhibits a combination of ordered (crystalline) and disordered (amorphous) regions. The degree of crystallinity can range from 40 to 70% depending on the source and extraction process. The amorphous regions have lower density and are more accessible with other molecules[17], [18]. Crystalline domains are generally more resistant to chemical, mechanical, and enzymatic treatments compared to the amorphous regions.

The molecular weight of cellulose is determined by the degree of polymerization (DP), which varies based on the extraction method and the source of cellulose. Bacterial cellulose typically has DP values ranging from 2000 to 6000, while plant cellulose contains approximately 10,000 glucopyranose units. Wood cellulose, on the other hand, consists of around 15,000 glucopyranose units[19], [20].

2.2 Cellulose nanocrystals

Nanocellulose fibrils can be extracted from wood-based fibers using mechanical methods that involve subjecting the pulp to high shear forces. This process breaks down larger wood fibers into nanofibers. Subsequently, cellulose nanocrystals (CNCs) can be isolated from the amorphous cellulose nanofibrils through acid-catalyzed hydrolysis[21]. CNCs are rod-like particles with nanoscale dimensions and exhibit a crystallinity index ranging from 54% to 88% [22]. The specific morphology of these nanoparticles depends on factors such as the origin of the CNC, the isolation procedure employed, and the parameters of the acid hydrolysis. For example, CNC derived from maize stalk residues typically have widths of 3-7 nm and lengths of 150-450 nm, while those obtained from sisal fibers have width of 8-16 nm and lengths of 122-272 nm. Conversely, CNCs sourced from tunicates display widths of 10-20 nm and lengths of 500-2000 nm [23]–[26]. Notably, CNCs are both biodegradable and nontoxic, making them environmentally friendly materials derived from renewable resources [16].

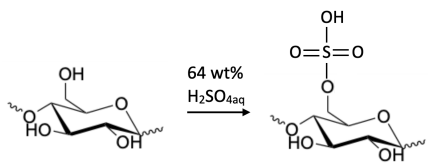

Figure 2.2: Hydrolysis of cellulose forming a sulfate half-ester moiety.

2.3 Modification of CNC

Cellulose is insoluble in water and organic solvents due to its intricate and structured assembly of polymer chains[27]. Consequently, cellulose nanocrystals (CNCs) require the introduction of surface charges or functionalization to achieve stability as colloidal particles. When produced through sulfuric acid hydrolysis, CNCs possess negative sulfate half-ester groups that decorate their structure (Fig.2.2). Research has indicated that these groups primarily attach to the C6 carbon sites of glucose residues, although attachment at the C2 and C3 sites is also feasible[28].

CNCs are generally characterized as hydrophilic, meaning they have a tendency to interact / mix with water. This hydrophilicity stems from the presence of hydroxyl (-OH) groups on the surface of CNCs, which have the ability to form hydrogen bonds with water molecules. These hydroxyl groups facilitate the dispersion of CNCs in water and enable them to interact effectively with aqueous environments. However, it is important to note that the hydrophilic or hydrophobic nature of CNCs can be altered through surface functionalization, allowing for modifications based on specific requirements.

The surface properties of cellulose nanocrystals (CNCs) can be customized by introducing different ions and components through functionalization. This process can reduce the inherent hydrophilicity of cellulose, increasing its compatibility with hydrophobic matrices. Various chemical treatments, such as silylation, mercerization, esterification, etherification, oxidation, benzoylation, graft copolymerization, and bacterial cellulose treatment, can be utilized to modify the surface of CNCs derived from different sources.[15], [29], [30].

2.4 Azetidinium salts

Azetidinium salts are used for the surface modification of cellulose nanocrystals due to their unique properties and potential applications. Firstly, azetidinium salts possess a reactive azetidine ring, which allows them to undergo nucleophilic substitution reactions with hydroxyl groups present on the cellulose nanocrystal surface. This enables covalent bonding between the azetidinium salts and cellulose, resulting in stable surface modification[31].

Secondly, the presence of azetidinium salts imparts desirable characteristics to the modified cellulose nanocrystals. These salts can introduce functionalities such as amino groups, carboxyl groups, or other chemical moieties, depending on the specific azetidinium salt used. These functional groups can enhance the dispersibility, stability, and compatibility of cellulose nanocrystals with various solvents and matrices[31]–[33].

2.5 Colloidal interactions of CNCs in aqueous suspensions

When cellulose nanocrystals are suspended in water, they form colloidal suspensions whose stability is influenced by various factors such as the particles' polydispersity, aspect ratio, and surface charge. The forces that affect these suspended particles determine their stability and the formation of liquid crystals. In general, it can be distinguished the DLVO and non-DLVO interactions between particles and surfaces.

2.5.1 DLVO theory

The DLVO (Derjaguin - Landau - Verwey - Overbeek) theory is a fundamental model to explain the stability of colloidal suspensions. It was proposed in the 1940s and explains that attractive interactions between particles result from van der Waals forces, while repulsive interactions result from electrostatic forces. The total potential energy between particles is the sum of these forces, and the stability of the colloidal suspension depends on the dominant force. Fig.2.3 graphically represents all interactions between CNC particles. The presence of an energy barrier between the primary and secondary minima plays a crucial role in determining the stability of colloidal particles. This energy barrier acts as a barrier that prevents the particles from coming into contact and aggregating. A larger energy barrier ensures greater stability of the suspension, as it hinders particle coagulation by preventing them from reaching the primary minimum. While particles may come into contact within the secondary minimum, the presence of Brownian motion can disrupt the formation of larger aggregates if the secondary minimum is not sufficiently deep.

The magnitude of the energy barrier is influenced by the surface potential of the particles and the ionic strength of the liquid medium. Higher surface potentials result in larger energy barriers, which contribute to more stable suspensions. Conversely, increasing the concentration of electrolytes reduces the energy barrier, potentially leading to decreased stability. The DLVO forces include van der Waals and double-layer interactions (electrostatic repulsion) [34], [35].

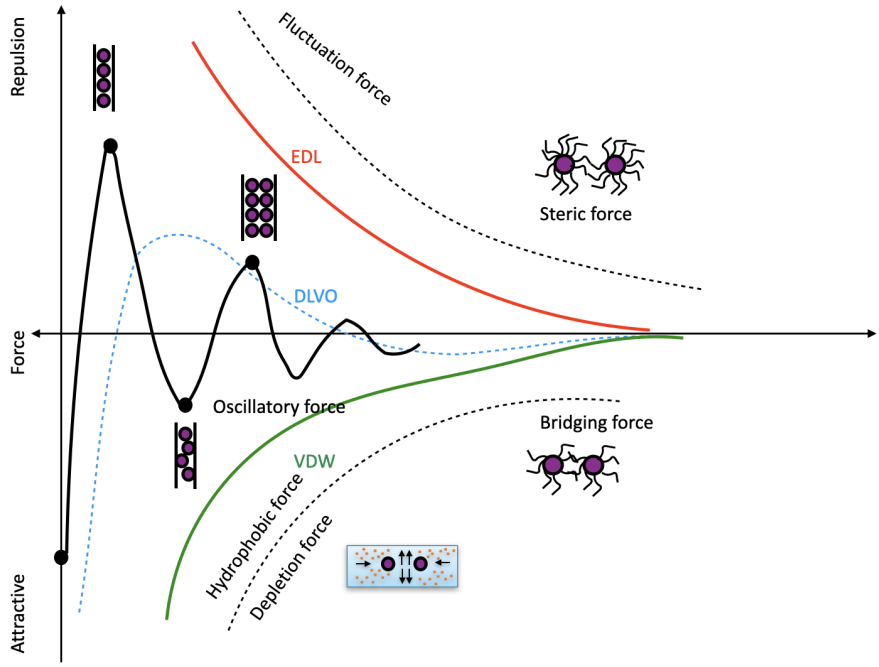

Figure 2.3: Schematic representation of force–distance profiles between particles and surfaces. The sign of van der Waaals (VDW) interaction depends on the varieties of interacting media. In turn, the electrostatic double layer (EDL) interaction can be repulsive or attractive between particles of the same or opposite charges. The classical DLVO forces include VDW and EDL interactions. In addition to DLVO forces, several other interactions including steric force, solvation forces (e.g., hydrophobic, hydration, and oscillatory structural interactions), bridging interaction, and depletion interaction can be named.

2.5.1.1 van der Waals forces

The interaction between particles in a colloidal suspension is affected also by attractive van der Waals forces [36]. These interactions are attractive forces that arise due to fluctuations in electron distributions within molecules or particles. They include London dispersion forces, which occur between all particles, and Keesom forces and Debye forces, which involve interactions

between particles with permanent dipoles and induced dipoles, respectively. Unless counteracted by opposing forces, van der Waals interactions have a tendency to induce the aggregation of colloidal particles.

2.5.1.2 Electrostatic Repulsion

CNCs typically possess charged surface groups, such as carboxylate or sulfate groups, which create electrostatic forces of repulsion between particles of the same charge. These repulsive forces act as a barrier, keeping the CNCs dispersed and maintaining the stability of the suspension. This repulsion prevents particles from coming into close proximity and helps to maintain suspension stability.

2.5.2 Non-DLVO interactions

Several other forces play a crucial role in stabilizing the CNC suspensions. For instance, hydrophobic effects, steric force, depletion force, bridging interaction, and hydration forces[34].

2.5.2.1 Hydrophobic interactions

Hydrophobic interactions play a crucial role in water suspensions, where hydrophobic molecules or particles tend to cluster together to minimize their contact with water. These interactions arise due to the tendency of water molecules to exclude hydrophobic entities, leading to the formation of aggregated structures. The hydrophobic effect is primarily driven by the entropy increase of water molecules surrounding hydrophobic surfaces, resulting in the entropic stabilization of the aggregates.[37]

2.5.2.2 Steric effects

CNC particles possess charged surface groups (e.g., carboxylate or sulfate) that create electrostatic repulsion between particles, preventing aggregation. This electrostatic repulsion acts as a steric stabilization mechanism, maintaining the stability of the suspension.

2.5.2.3 Depletion forces

Depletion forces are type of attractive interactions that arise in water suspensions containing large colloidal particles or macromolecules. When smaller particles or solutes are present, they create a "depletion zone" around the larger entities due to the excluded volume effect, causing the larger particles to experience an attractive force that drives them together.

2.5.2.4 Bridging interactions

Bridging forces arise between two surfaces, when one of the surface or particle adsorbs onto the surface of larger particles, creating bridges between them. These bridges lead to the formation of strong, interconnected networks that enhance the stability and mechanical properties of the suspension.

2.5.2.5 Hydration forces

The hydration shell (forces) refers to the layer of water molecules that surround the CNC particles[38]. When CNCs are dispersed in water, water molecules are attracted to the charged surface groups on the CNCs. These water molecules form a dynamic and structured layer around the particles, known as the hydration shell. The hydration shell refers to the layer of water molecules surrounding an ion or molecule in an aqueous solution [39].The hydration shell plays a crucial role in stabilizing the CNC suspension by providing electrostatic shielding, preventing particle aggregation, and maintaining colloidal stability.

2.6 CNC phases

Based on combination of all these factors above and additional ones (concentration, aspect ratio, pH, solvent), cellulose nanocrystals self-assembling (i) or non-self-assembling (ii). Self-assembling occurs when the attractive forces, such as van der Waals or hydrogen bonding, outweigh the repulsive forces present in the system. On the other hand, CNCs can aggregate under certain conditions where the repulsive forces are insufficient to counteract attractive forces. Aggregation can lead to the formation of larger clusters or flocs, resulting in reduced dispersion and colloidal stability.

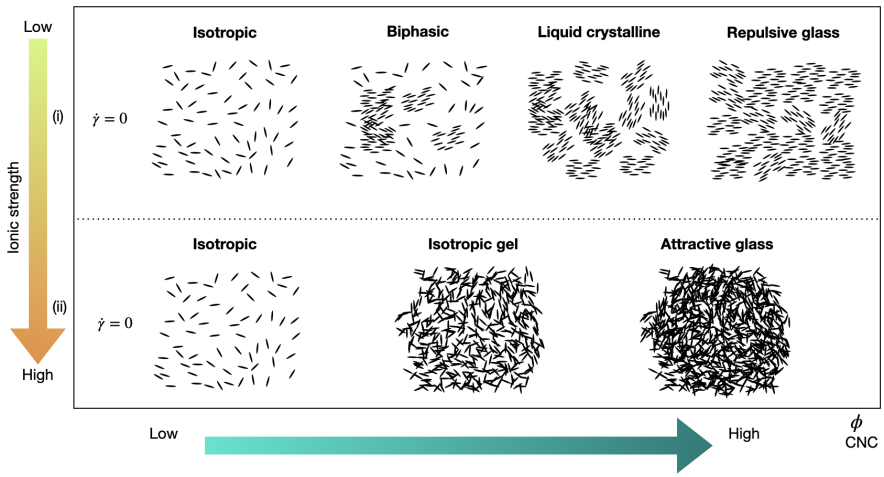

Figure 2.4: Phase diagram of aqueous CNC suspensions as a function of CNC concentration and ionic strength: (i) self-assembling CNC, (ii) non-self-assembling CNC.

The phase diagram presented in Fig.2.4 depicts the different phases observed in aqueous cellulose nanocrystal (CNC) systems at varying ionic strengths. At low concentrations, CNC suspensions form an isotropic phase, while above a certain threshold, they transition into a biphasic system with coexisting isotropic and liquid crystalline domains (Fig.2.4 (i)). Further concentration increase leads to the formation of a complete liquid crystalline phase, which can exhibit nematic and/or chiral nematic structures. The chiral nematic phase is characterized by its pitch, representing the distance between aligned nanorods after a 360°rotation, while the nematic phase indicates long-range orientational order compared to the dimensions of the nanorods[16], [40]. If the concentration continues to rise, the liquid crystalline phase may transform into a repulsive glassy state.

On the other hand, non-self-assembling CNC suspensions in dilute aqueous solutions (Fig.2.4 (ii)) exhibit an isotropic phase under static conditions, but aggregation occurs with increasing concentration, eventially resulting in the formation of an isotropic gel phase. Further concentration increase leads to reduced inter-particle distance and jamming into an attractive glass phase[41].

2.7 Optical properties

Under appropriate conditions, CNCs orient to form liquid crystal phases exhibiting remarkable optical properties. The self-assembly process leads to the alignment of CNCs along a preferred direction, resulting in anisotropic optical properties. One consequence of CNC assembly is the emergence of birefringence, which refers to the double refraction of light passing through the material. The aligned CNCs induce anisotropy in the refractive index, causing light to split into two orthogonal polarization components with different velocities[42]. This birefringence can be observed by polarized light microscopy, where CNC suspensions appear as colourful patterns.

The optical properties of CNCs assemblies strongly depend on the degree of CNCs alignment and the concentration of CNCs in the suspension. Higher CNC concentrations and more substantial alignment enhance birefringence and more pronounced optical effects. These unique optical properties make CNCs assemblies promising candidates for various applications, including optical coatings, displays, and sensors [43], [44]. The ability to precisely control CNCs assembly and exploit their optical properties opens up exciting opportunities for developing advanced materials with enhanced performance and functionality.

CHAPTER 3

Materials

The materials under study have been categorized into two groups, each exhibiting differences in their sulfate group content, concentrations, aspect ratio and the type of ions added to the -SO_3^- group. These two scenarios were selected as case studies to distinguish between self-assembling and non-self-assembling aqueous systems. The suspensions were analyzed using various techniques to detect any changes in their microstructure.

3.1 Self-assembling CNC suspensions

3.1.1 Commercial CNCs

To conduct the study outlined in Papers I, II, cellulose nanocrystals were purchased from CelluForce, based in Montreal, Canada. These nanocrystals were obtained by subjecting cellulose to sulphuric acid hydrolysis and resulted in a spray-dried powder, neutralized with Na^+, that could be dispersed in water. The sulfate content of these nanocrystals was roughly 250 μmol/g, and their reported length ranged from 100 to 300 nm, with a diameter of 4.1 $\pm$ 1.0 nm [45], [46]. As a result, their aspect ratio was between 25 and 75.

In Paper I, suspensions with concentrations ranging from 2 to 9 wt% were prepared by immersing the nanocrystals in deionized water using a Millipore Milli-Q Purification System. The mixture was then stirred on a bench shaker for a duration of 24 hours.

For Paper II, a CNC concentration of 2 wt% was prepared using Milli-Q water from the Millipore Milli-Q Purification System. The suspension was dispersed through microfluidization using an M110-EH instrument at a pressure of 1700 bar for a single pass. Afterwards, the suspension underwent filtration twice, using Munktell FiltrakTM grade 3 papers from Fischer Scientific.

Subsequently, the 2 wt% CNC stock suspension was gently evaporated at room temperature while being stirred magnetically until it reached a concentration of 10.2 wt%. From this 10.2 wt% suspension, concentrations of 2, 3, and 5 wt% CNC were prepared by diluting it with deionized water from the Millipore Milli-Q Purification System. The dilution process took place at room temperature with magnetic stirring for a duration of 24 hours.

3.1.2 Desulfated CNCs

Low-charge cellulose nanocrystal (CNC) studied in Paper II suspensions were prepared following a previously reported acid-catalyzed desulfation method [47]. The initial stock suspension contained 2 wt% CNCs in their sodium form. To convert the CNCs from their acid-form desulfated state back to the sodium form, NaOH was added until the pH reached 7. The suspension was then concentrated to a final concentration of 1.45 wt%. Further dilutions were carried out by adding Milli-Q water to the 1.45 wt% CNC suspension. This resulted in the preparation of suspensions with concentrations of 0.5 wt% and 0.73 wt%.

3.1.3 Low sulfated CNCs with different counterions

To prepare the aqueous suspension of CNC-OSO_3H for Papers III, IV, and V, a solution of 64 wt% sulfuric acid was used to acid hydrolyze MCC. The mixture was continuously stirred at 45°C for two hours. Once hydrolysis was complete, the suspension was dialyzed against deionized water until the conductivity of the effluent stabilized below 5 μS/cm. The CNC slurry was then dispersed in DI water through sonication under cold conditions, resulting in a stable colloidal suspension with a concentration of 2 wt%.

Subsequently, autocatalyzed desulfation [48] was employed to produce CNCs with low sulfate content, known as CNC^{L}-OSO$_3$H. A 200 mL batch of CNC with a dry content of 2 wt% was heated to 70 °C for two hours [48]. After desulfation, the suspensions were subjected to potentiometric titration, and the sulfate content was measured to be 170 ± 17 μ mol/g. Then, CNCs with different counter ions were prepared by ion-exchange reactions by replacing H^+ from sulfate groups with Lithium (Li^+), Sodium (Na^+), Potassium (K^+), Triethyl ammonium [$N^+H(C_2H_5)_3$], Triethanol ammonium [$N^+H(C_2 2H_5OH)_3$] ions and corresponding CNC samples were named as CNC-OS$_3$Li, CNC-OS$_3$Na, CNC-OS$_3$K, CNC-OS$_3$TEtOA, and CNC-OS$_3$TEtA, respectively. The amount of bases was added in the same mol equivalent ratio as the concentration of sulfate groups.

3.1.4 CNCs with different aspect ratio

The CNC suspensions used for Paper VI were obtained from the USDA Forest Lab at the University of Maine. The fractionation process followed a similar procedure outlined in a previous study by Honorato-Rios et al. (2020) [49]. To prepare the initial CNC suspension, the received CNCs diluted by adding pure water. The CNC suspension was then sonicated using an ultrasonic probe with a 7 mm tip diameter. Next, the initial CNC suspension, with a global mass fraction of 4 wt%, was placed in a separator funnel and sealed. After one week of undisturbed settling, anisotropic and isotropic phases separated. The anisotropic phase, composed of the long CNC fraction, was decanted into a beaker by opening the stopcock. The short rod sample, another 400 g of the initial CNC suspension, was filled into a second separatory funnel and left standing for three weeks. After the separation occurred, the anisotropic phase was discarded by opening the stopcock and decanting it into a beaker. The sample containing the isotropic supernatant with the short rod fraction was retained. For each fraction 4 concentrations were prepared.

3.2 Non-self-assembling CNC suspensions

3.2.1 Highly sulfated CNCs

To perform the experiments described in Paper III, suspensions of pristine CNC with higher sulfate content and a different counter ion compared to com-

mercial CNCs were created by subjecting microcrystalline cellulose (MCC) to acid hydrolysis with sulfuric acid H_2SO_4, using a method outlined by Hasani et al. [50]. The resulting CNC-SO_3H had a sulfate content of 330 μmol/g. The concentration of this stock suspension was 5.7 wt%. Deionized water (Millipore Milli-Q purification system) was used to dilute the stock suspension and obtain 6 different concentrations of pristine CNC (pCNC) suspensions: 1, 1.5, 2, 3, 4, and 5 wt%. For Paper V, the acid hydrolysis of MCC was performed using a solution of 64 wt% H_2SO_4. The mixture was stirred continuously at 45°C for a duration of two hours. After the hydrolysis process was completed, the suspension was subjected to dialysis against deionized water until the conductivity of the effluent reached a stable value below 5 μS/cm. Subsequently, the CNC slurry was dispersed in DI water through cold sonication, resulting in the formation of a stable colloidal suspension with a concentration of 2 wt%. The sulfate content present on the CNCs was determined through potentiometric titration and measured as 275 μmol/g.

3.2.2 Surface modification with azetidinium salts

In Papers III and IV were CNC with dialkylamines surface groups evaluated. Two ways of modification was performed. (i) synthesis of 1-chloro-2-hydroxy-propyl-N-dialkylamine (open form) and, (ii) synthesis dialkylamine azetidinium salts molecules (Closed form). Microcrystalline Cellulose (MCC) PH-101, Sulfuric Acid (98 wt%), Undecanal, Methylamine (MeOH-solution), Nonanal, Propylamine, Hexyl amine, 2-Ethyl hexyl amine, Epichlorohydrin, Magnesium Sulfate, Sodium Borohydride Ethanol, Tetrahydrofuran, Chloroform, and Isopropanol were purchased from Sigma Aldrich. Secondary amines were synthesized by reductive amination of aldehydes with primary amines, Fig.3.1 The synthesis of 1-chloro-2-hydroxy-propyl-N-dialkylamines involved

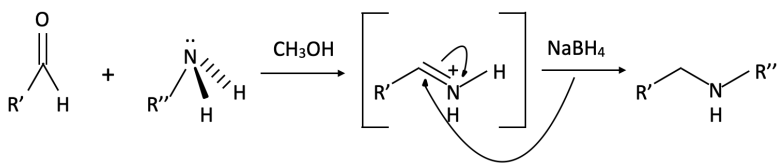

Figure 3.1: Mechanism of secondary amines by reductive amination of aldehydes with primary amines.

the following steps:

- solution containing isopropanol (IPA) and Epichlorohydrin was prepared and stirred. Dialkylamine was then added to the solution while stirring. The reaction mixture was continuously stirred for 36 h at room temperature using a magnetic stirrer.
- Afterward, the solvent was removed through rotary evaporation, and a portion of the crude product was analyzed using NMR, which confirmed the presence of the open form of azetidinium molecules.
- To further process the crude product, it was dissolved in a mixture of H2O:IPA and stirred at room temperature for 30 minutes. Subsequently, the temperature was raised to 90 °C, and the reaction was allowed to proceed for 2 h.
- The solvent was then evaporated using a rotary evaporator, and the resulting product was characterized by NMR, indicating the formation of the closed form of azetidinium molecules.

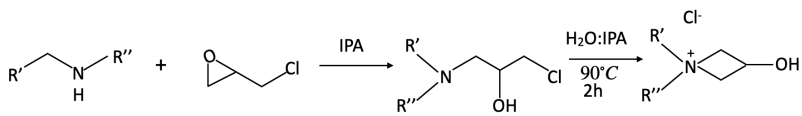

Figure 3.2: The process involves the reaction of a secondary amine with epichlorohydrin, leading to the formation of 1-chloro-3-amino propan-2-ol through ring opening. Subsequently, this intermediate is converted into 3-hydroxyazetidinium chloride through ring closure.

- Then, the conjugation of azetidinium salt to sulfate half-ester was performed by heating the mixture at 90 °C for 4 h. When the reaction had been completed, the mixture was cooled to room temperature. The reaction mixture was transferred into dialysis tubing and dialyzed against deionized water for 48 h to remove unreacted azetidinium reagent.

Preparation of films

In addition to analyzing suspensions, Paper VI involved the characterization of multiple films. These films were formed by casting 2 wt% of each fraction of

CNC into 35 mm diameter polystyrene Petri dishes. Subsequently, the films were allowed to dry for 36 hours under ambient conditions (20 °C, 40-50% relative humidity).

CHAPTER 4

Methods

4.1 Molecular characterization

Molecular characterization enables the acquisition of valuable insights regarding the chemical or molecular properties of a given sample, including details about its chemical structures, composition, and surface charge.

4.1.1 ATR-FTIR

Fourier Transform Infrared Spectroscopy (FTIR) provides information about functional groups in a sample. ATR-FTIR was recorded on a Perkin Elmer Frontier FT-IR Spectrometer (Waltham, MA, USA) equipped with a diamond GladiATR attenuated total reflectance (ATR) attachment from Pike Technologies. The different measurements were done with the attenuated total reflectance (ATR) technique, and the spectra were recorded between 4000 and 400 cm^{-1}, with 32 scans being collected with a resolution of 2 cm^{-1}.

4.1.2 Nuclear Magnetic Resonance Spectroscopy (NMR)

Nuclear Magnetic Resonance (NMR) spectroscopy is analytical technique that provides detailed information about the molecular structure and chemical composition of a sample. By analyzing the NMR signals produced by atomic nuclei, NMR can reveal valuable insights into bonding patterns, molecular dynamics, and interactions within the sample. This spectroscopy analysis was used to evaluate the structure of the synthesized molecules in Paper III and IV. ^{1}H NMR was done for all samples and ^{13}C NMR when necessary. Samples for NMR were prepared by dissolving the salts in 0.7 mL of chloroform-d ($CDCl_3$) or dimethyl sulfoxide (DMSO) in an NMR tube. NMR analysis was conducted with a Varian 400-MR (Agilent). Spectra were analyzed with a MestReNova 11 (Mestrelab S.L, Santiago de Compostela, Spain).

4.1.3 Zeta potential (ζ)

Zeta potential (ζ) refers to the electric potential difference between the surface of a particle or colloidal dispersion and the surrounding liquid medium. It is a measure of the net charge on the particle's surface and provides valuable information about the stability and behavior of colloidal systems. Zeta potential measurement helps in understanding the electrostatic forces that influence particle aggregation, dispersion, and interactions with other particles or surfaces, which in turn affects various properties such as dispersion stability, sedimentation, and surface adhesion. Zeta potential measurements of CNC suspensions were performed using a Zetasizer Nano ZS (Malvern Instruments, UK) and DTS1070 folded capillary cells. CNC suspensions were diluted 0.01 wt%, at an NaCl concentration of 1 mM, which was added to compress the electrical double layer[51], [52]. All measurements were conducted at 25 °C, with a stabilization time of 120 s, repeated 3 times and the average value was reported.

4.1.4 Dynamic Light Scattering (DLS)

Dynamic Light Scattering (DLS) is a technique used to measure the size distribution of particles or molecules in a solution by analyzing the fluctuations in scattered light caused by their Brownian motion. DLS provides information about the hydrodynamic diameter of the particles, which includes both the size and the solvent's effect on their motion. DLS measurements of CNC

suspensions were performed using a Zetasizer Nano ZS (Malvern Instruments, UK) and DTS1070 folded capillary cells. CNC suspensions were diluted to 0.001 wt% for DLS. Similar as for zeta potential, 1mM of NaCl was added to compress the double layer. All measurements were conducted at 25 °C, with a stabilization time of 120 s, repeated 3 times and the average value was reported.

4.1.5 Titration

Titration is a technique used to determine the concentration of a substance in a solution by reacting it with a standardized solution of another substance (known as the titrant) of known concentration. The measurement in titration typically involves the gradual addition of the titrant to the analyte until the reaction between the two is complete, which is indicated by a noticeable change in a measurable property, such as pH or color. For Papers II-V surface charge was measured by titration of acid-form CNC suspensions in the presence of NaCl against NaOH. The inflection point from the titration can be related to the surface charge density of crystallites [53], i.e. percent sulfur content by weight, calculated as:

$$\%S \equiv \frac{V_{NaOH} C_{NaOH} M_w(S)}{m_{susp} C_{susp}} \times 100\% \tag{4.1}$$

where V_{NaOH} corresponds to the volume of NaOH at the equivalence point, C_{NaOH} is the concentration of NaOH used to the titration, $M_w(S)$ refers to the molecular weight of sulfur, and m_{susp} and C_{susp} are the mass and concentration of the suspension, respectively.

4.2 Material characterization

4.2.1 Atomic Force Microscopy (AFM)

Atomic Force Microscopy (AFM) is a high-resolution imaging technique that measures the topography and surface properties of materials at the nanoscale. It employs a sharp probe attached to a cantilever that scans the surface, and the interaction forces between the probe and the sample are measured. AFM provides detailed information about surface roughness and morphology. Semi-contact mode atomic force microscopy (AFM, NTEGRA, NT-MDT,

Russia) with Tap300AI-G tips were used for morphology characterization of the CNCs. Poly-L-lysine solution was deposited on a freshly cleaved mica surface (NanoAndMore GmbH). Subsequently, the mica surface was rinsed with ultrapure water and dried under nitrogen gas flow. 150 μm of 0.001 wt% CNC suspensions were deposited on a mica substrate. Next, the surface was washed off with deionised water and dried under nitrogen gas flow. The samples were dried in the oven for 30 min at 50 °C. After removing polynomial backgrounds and aligning the rows of 5 x 5 µm images, Gwyddion 2.56 software was used to extract single CNCs. These profiles were then baseline-corrected using the polynomial fitting, and their height was determined from the resulting profile.

4.2.2 Transmission Electron Microscopy (TEM)

Transmission Electron Microscopy (TEM) is an imaging technique that uses a beam of electrons to visualize the internal structure of specimens at high resolution. TEM measures the interaction of the electron beam with the sample, allowing for the observation of fine details. Samples for Paper II and VI were prepared using distinct methods to align with the specific objectives of each study. For Paper II which objective was on determining the differences between structures sulfated and desulfated CNCs, small droplets of the CNC suspensions were frozen in liquid ethane/propane, then transferred to a freeze substitution AFS2 FSP equipment chamber (Leica, Wetzlar, Germany) kept at -90 °C. Water is substituted with acetone at -40 °C. The resin was polymerized at -40 °C using UV-light and ultrathin sections of 60 nm of each sample was performed using a Diatome ultra diamond knife (Diatome, Hatfield, PA, United States) in a Powertome XL ultramicrotome (RMC products, Boeckeler Instruments Inc., Tucson, Arizona, United States). In turn, for Paper VI, where the aim was to estimate the lengths and width for particular CNCs fractions, 0.001 wt% CNC suspension was placed on a carbon-coated copper grid prepared by glow discharge and staining with uranyl acetate solution. TEM images were obtained using a Talos F200X G2 microscope (FEI) operated at 200 kV and a CCD camera.

4.2.3 Thermal properties

One of the methods to evaluate the thermal stability and degradation processes of materials is Thermogravimetric Analysis (TGA). This technique is

used to determine the changes in weight of a sample as a function of temperature or time. For Papers III-V, thermal analysis was carried out using the TGA/DSC 3 + Star system from Mettler Toledo (Switzerland). The temperature range of the samples was 30 to 500 °C, with a 10°C/minute heating rate.

4.2.4 POM

Polarized optical microscopy (POM) is a technique used to observe and analyze the optical properties of materials under polarized light. It involves the use of polarizing filters to control the direction of light and reveal valuable information about the sample's birefringence, crystal structure, and optical anisotropy. Transmission optical microscopy was carried out with a Carl Zeiss A1 (Oberkochen, Germany) optical microscope equipped with linear polarizers in cross-polarizer setup. For Paper II, a 530 nm phase retardation plate was inserted into microscope to help distinguish phase transitions for desulfated CNC suspensions. A birefringent material can influence the polarization of light by altering its ellipticity and the primary oscillation direction. In the "bright" state, the director/optic axis aligns the light leaving the liquid crystal in a linearly polarized manner, matching the direction transmitted by the exit polarizer (analyzer), allowing light to pass through. Conversely, in the "dark" state, the director reorients to eliminate the birefringence effect, keeping the light's polarization unchanged and perpendicular to the transmission direction of the analyzer, resulting in light absorption[54].

The observable consequence of birefringence is often a display of colors rather than just bright or dark. This is because the polarization change that light undergoes while passing through the liquid crystal depends on its wavelength (color). As a result, when a liquid crystal is placed between crossed polarizers and illuminated by white light, it frequently exhibits vibrant colors. The specific color observed is influenced by the magnitude of the birefringence and the thickness of the sample.

In Paper VI, the films that were cast underwent further characterization using micro-spectroscopy. This involved utilizing a fiber-optic cable with a core diameter of 100 μm to obtain spectra that corresponded to the images captured through POM.

Figure 4.1: Viscous element: dashpot (left) and elastic element: spring (right).

4.3 Rheological characterization

The study of the deformation and flow of materials is known as rheology. The word "rheology" originates from the Greek words $\rho\varepsilon\omega$ *rhéō*, meaning "flow", and -$\lambda o\gamma i\alpha$, meaning "study of". Therefore, it means "study of flow". This term was first used by Eugene C. Bingham in 1920 [55]. Rheological characterization is important in quantifying and understanding the relationship between deformation and stress. The most significant material factors affecting the rheology of suspensions are weight percentage, aspect ratio, particle interactions, and phase separation. Rheological properties are crucial for quality control, industrial processing methods, and end-use applications [56].

4.3.1 Introduction to viscoelasticity

Suspensions are heterogeneous systems comprising at least two immiscible phases. They are considered complex fluids that demonstrate viscoelastic behavior across a broad range of compositions. Viscoelastic fluids possess both viscous and elastic properties during flow. The behavior of a viscoelastic material can be illustrated by combining the models of an ideal viscous fluid and an ideal elastic solid, as shown in Figure 4.1.

A dashpot, which follows Newton's viscosity law, can be utilized to model an ideal viscous fluid. According to this law, the shear stress is proportional to the rate of shear deformation, with the viscosity η serving as the proportionality constant, as expressed in Equation 4.2 where γ represents the shear strain and $\dot{\gamma} = d\gamma/dt$ is the shear rate. On the other hand, an ideal elastic solid, as defined by Hooke, depicts the shear stress σ as proportional to the shear strain γ, with the shear modulus G serving as the proportionality constant, as shown in Equation 4.3

$$\sigma = \eta \frac{d\gamma}{dt} \tag{4.2}$$

$$\sigma = G\gamma. \tag{4.3}$$

The most straightforward mechanical viscoelastic models are formed by connecting the dashpot and spring in series (as shown in Fig. 4.2). When the spring and dashpot are connected in series, a Maxwell element is formed, which is frequently used to describe fluids. In the Maxwell viscoelastic model,

Figure 4.2: Maxwell element.

the stress in the spring and dashpot components is equivalent, denoted as σ_s and σ_d, respectively, and the overall strain is the summation of the individual strains:

$$\sigma = \sigma_s = \sigma_d \tag{4.4}$$

$$\gamma_t = \gamma_s + \gamma_d \tag{4.5}$$

Consequently, a Maxwell element's total shear rate $\dot{\gamma}$ is the sum of the individual shear rates.

$$\dot{\gamma}_t = \dot{\gamma}_s + \dot{\gamma}_d \tag{4.6}$$

Introducing Newton's and Hooke's laws, Eq. (4.2) and (4.3), in Eq. 4.6 results in

$$\frac{d\gamma}{dt} = \frac{\sigma}{\eta} + \frac{1}{G}\frac{d\sigma}{dt} \tag{4.7}$$

By defining $\lambda_M = \eta/G$, as the relaxation time, the Maxwell model can be rewritten as:

$$\lambda_M \dot{\sigma} + \sigma = \eta\dot{\gamma} \tag{4.8}$$

4.3.2 Linear and nonlinear viscoelasticity

Dynamic shear oscillatory measurements involve applying a sinusoidal deformation to a material and measuring the stress response as a function of time [57]. Such measurements can be categorized into linear and nonlinear viscoelastic regimes. In linear viscoelastic oscillatory shear tests, as shown in

Fig. 4.3(a), a sinusoidal strain input is applied to the material,

$$\gamma(t) = \gamma_0 \sin(\omega t) \tag{4.9}$$

where γ_0 is the strain amplitude and ω the angular frequency, where $\omega = 2\pi f$ and f is the applied frequency, results in a sinusoidal shear stress output

$$\sigma(t) = \sigma_0 \sin(\omega t + \delta) \tag{4.10}$$

where δ is the phase angle and σ_0 is the shear amplitude. The time-dependent shear rate is therefore

$$\dot{\gamma}(t) = \gamma_0 \omega \cos(\omega t) \tag{4.11}$$

The shear modulus takes a complex form:

$$G^* = \frac{\sigma(t)}{\gamma(t)} = \frac{\sigma_0}{\gamma_0}(\cos\delta + i\sin\delta) = G' + iG'' \tag{4.12}$$

as represented in Fig. 4.4, where G' refers to storage modulus and G'' to loss modulus.

The storage modulus, G', is the elastic contribution and it can be defined as

$$G' \equiv \frac{\sigma_0}{\gamma_0}\cos\delta \tag{4.13}$$

and the loss modulus which is the viscous contribution

$$G\text{”} \equiv \frac{\sigma_0}{\gamma_0}\sin\delta \tag{4.14}$$

In turn, the ratio of loss modulus and storage modulus is called loss tangent (tanδ), representing the damping in materials:

$$\tan\delta = \frac{G''}{G'} \tag{4.15}$$

The situation differs in the nonlinear viscoelastic regime, where the shear stress response is non-sinusoidal. Consecutively, the Fourier spectrum of the shear stress $\Sigma(\omega)$, in linear viscoelastic oscillatory shear, contains the contribution of the imposed excitation, $I_1(\omega/\omega_i = 1)$, where ω_i is the angular frequency of the excitation (Fig.4.3. Therefore, higher harmonics, I_n, $n = 3, 5...$,

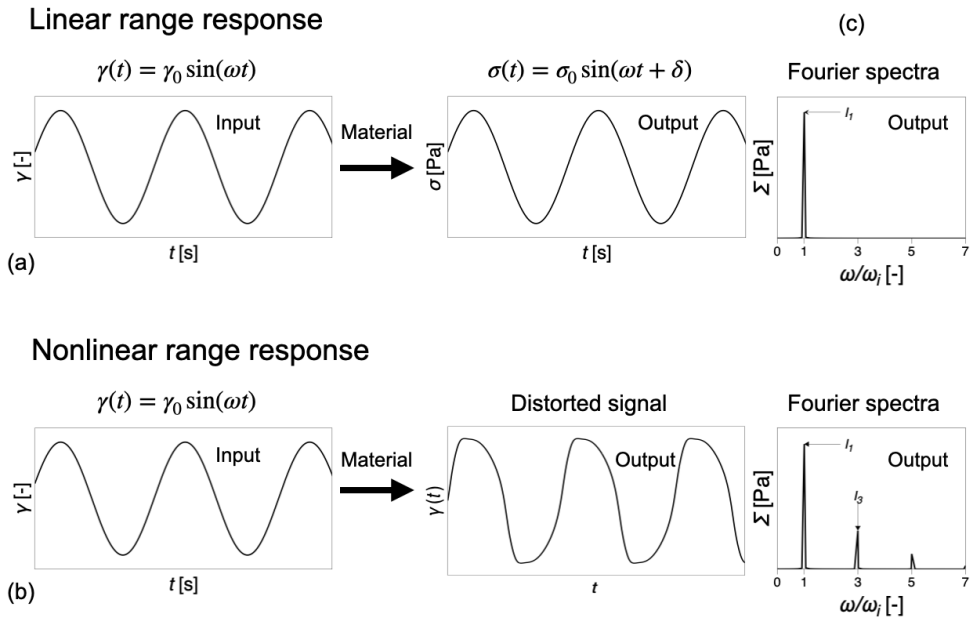

Figure 4.3: Schematic illustration linear and nonlinear time-dependent strain inputs (a) and linear and nonlinear stress outputs (b) and their corresponding Fourier spectra (c).

are revealed in the corresponding Fourier spectra in addition to the fundamental intensity I_1 [58]. The third relative higher harmonic, $I_{3/1} \equiv I_3/I_1$, can be used to characterize the shear stress signal nonlinearity, as I_3 contains the largest nonlinear contribution to the spectra [58], [59].

Experimental data from strain sweep measurements at constant ω are compared in Fig. 4.5. The data shows three viscoelastic regions: (i) small amplitude oscillatory shear (SAOS), (ii) medium amplitude oscillatory shear (MAOS), and (iii) large amplitude oscillatory shear (LAOS). In the SAOS region, the response is in the linear regime, and G' and G'' are independent of the applied γ_0. The nonlinear parameter $I_{3/1}$ is scattered and exhibits a general decay scaling behavior of $I_{3/1} \propto \gamma_0^{-1}$, which is attributed to nonlinearities caused by instrumentation noise [59], [60]. The MAOS region marks the beginning of nonlinearity and is characterized by a steep increase in $I_{3/1}$

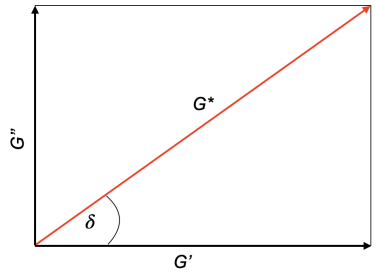

Figure 4.4: Representation of the complex shear modulus.

[61], where $I_{3/1} \propto \gamma_0^2$. However, for higher strain amplitudes, i.e., LAOS, the quadratic scaling is lost. Fig. 4.5 also shows that the dynamic range of $I_{3/1}$ spans approximately three decades compared to less than one decade in G' and G''. Therefore, Fourier Transform Rheology (FT-R) is a more sensitive technique for nonlinear analysis, capable of detecting changes in microstructure that are not observable through linear analysis.

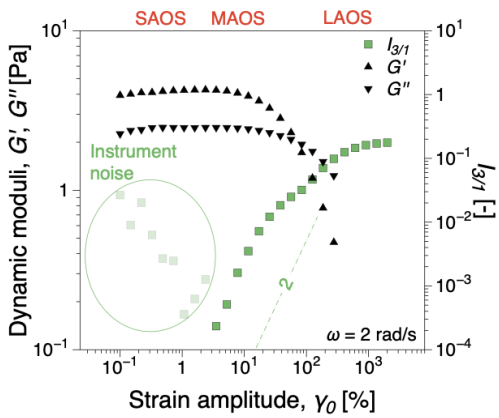

Figure 4.5: Experimental data from strain sweep measurement at constant angular frequency illustrating the linear and nonlinear viscoelastic regimes. The dynamic moduli, G' and G'' and the third relative higher harmonic, $I_{3/1}$ are compared.

4.3.2.1 Stress decomposition analysis

The material's nonlinear response can be visually represented using elastic and viscous Lissajous-Bowditch (LB) diagrams, as shown in Figure 4.6. These diagrams plot the normalized stress ($\sigma(t)/\sigma_{max}$) against the normalized strain ($\gamma(t)/\gamma_0$) for the elastic LB, and against the normalized shear rate ($\dot{\gamma}(t)/\dot{\gamma}_0$) for the viscous LB. In linear viscoelastic behavior, the response is elliptic in shape, while any distortions or deviations from an ellipse indicate a nonlinear viscoelastic material response [58]. Elastic and viscous material parameters can be derived from the LB diagrams to quantify the intracycle material behavior [62].

$$G'_M \equiv \left.\frac{d\sigma}{d\gamma}\right|_{\gamma=0} \tag{4.16}$$

$$G'_L \equiv \left.\frac{\sigma}{\gamma}\right|_{\gamma=\gamma_0} \tag{4.17}$$

$$\eta'_M \equiv \left.\frac{d\sigma}{d\dot{\gamma}}\right|_{\dot{\gamma}=0} \tag{4.18}$$

$$\eta'_L \equiv \left.\frac{\sigma}{\dot{\gamma}}\right|_{\dot{\gamma}=\dot{\gamma}_0} \tag{4.19}$$

Consequently, the strain-stiffening (S) and shear-thickening (T) dimensionless ratios [62] can be defined as:

$$S \equiv \frac{G'_L - G'_M}{G'_L} \tag{4.20}$$

$$T \equiv \frac{\eta'_L - \eta'_M}{\eta'_L} \tag{4.21}$$

where $S>0$ indicates intracycle strain-stiffening, $S<0$ intracycle strain-softening, $T>0$ intracycle shear-thickening and $T<0$ intracycle shear-thinning.

4.3.3 Linear and nonlinear measurements

Oscillatory shear experiments, both linear and nonlinear, were conducted on an Anton Paar MCR 702 TwinDrive and 702e MultiDrive rheometers (Graz, Austria) in strain-controlled mode using a parallel plate geometry with a 50

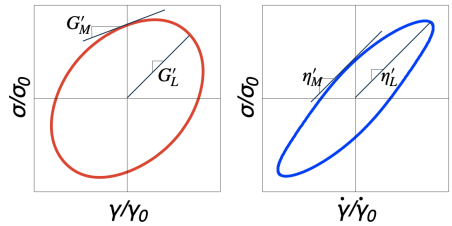

Figure 4.6: Elastic (left) and viscous (right) Lissajous-Bowditch diagrams and associated material nonlinear parameters.

mm diameter and 1 mm gap. The temperature was maintained at 23 °C throughout all the experiments. Prior to the measurements, a relaxation period of 300 s was allowed for each sample after it was positioned at the 1 mm gap. The strain sweep tests were performed over a range of 0.01 to 1500% at frequencies of 0.6, 1, 2 and 4 rad/s for all publications. In addition, the frequency sweep tests were carried out between 0.01 to 600 rad/s at a fixed strain amplitude, which was selected based on the linear viscoelastic region obtained from the strain sweep tests.

4.3.4 Rheo-PLI

A custom rheo-optical visualization setup based on the P-PTD200/GL accessory with a transparent parallel-plate geometry (43 mm diameter) was used for rheological polarized light imaging experiments (rheo-PLI) in a single motor transducer configuration. Two linear polarizers were placed at 45 ° and 90 ° relative orientation above and below the parallel-plate setup. A Canon DSLR camera setup comprising a Canon L-series 100 mm macro lens combined with a Canon 25 mm extension tube was used for HD video recordings (1,280x720; 60 fps) from below, perpendicularly to the shear plane. Space-time diagrams were constructed from the video recordings by taking out one line of pixels at a fixed position out of each still frame and appended to a new image having the x-dimension corresponding to the experimental time and the y-dimension corresponding to the length L, as shown in Fig. 4.7. Both oscillatory and steady shear measurements were performed, but strain sweep measurements were only done at 0.6 and 4 rad/s with a strain amplitude range of 0.01 to

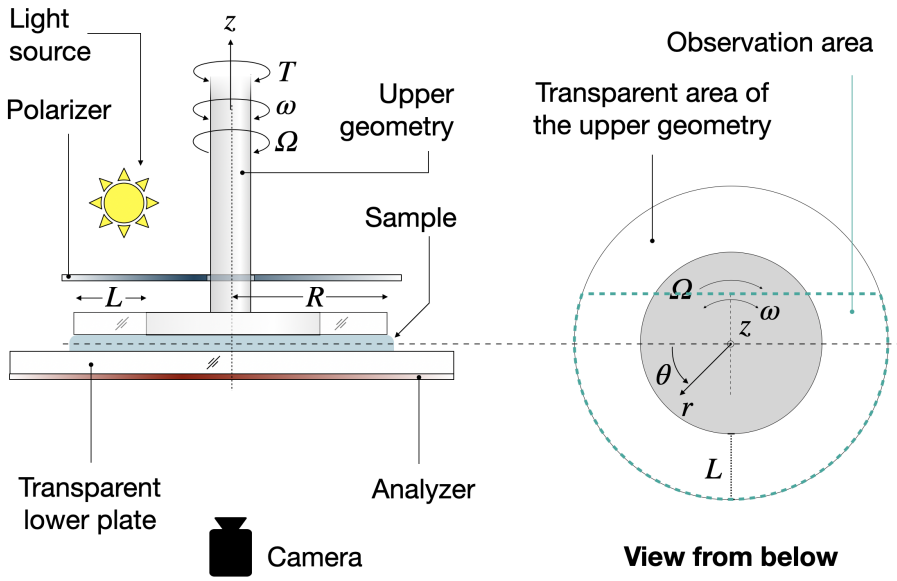

Figure 4.7: Schematic overview of the combined rheology polarized light imaging (rheo-PLI) setup [63].

1500%. Steady shear measurements were conducted within the shear rate range of 0.001 to 100 s^{-1} using a custom steady-state detection procedure [63].

This characterization allows to visualize the Maltese - cross signature and colorful pattern, while applying shear deformation. A birefringent materials, such as cellulose nanocrystals appear bright or dark between crossed polarizers depending on the orientation of its optic axis (or director) relative to the polarizer and analyzer.

When the optic axis of a birefringent material aligns parallel to the transmission axis of crossed polarizers (i.e., polarizer and analyzer aligned), the material appears bright as it doesn't significantly alter the polarization of light passing through, allowing light to easily transmit through both polarizers. On the other hand, when the optic axis is oriented perpendicular to the transmission axis of crossed polarizers (i.e., polarizer and analyzer crossed at 90 °), the material appears dark due to the birefringence effect, which changes

the polarization of light, preventing its transmission through the analyzer.

However, the visible effect of birefringence is usually more than just bright or dark; it often manifests as colors [54]. The observed colors when illuminated with white light depend on the material's thickness and the degree of order of the liquid crystals within it. Another crucial factor influencing the color is the applied shear rate. The rheo-PLI technique demonstrated that the color of cellulose nanocrystal suspensions is also affected by the deformation caused by applying shear rates. Hence, a combination of these factors contributes to the colorful appearance of birefringent materials.

4.3.4.1 Anisotropy and its consequences on the viscosity

The anisotropic viscosity of liquid crystals, including cellulose nanocrystals, refers to their directional dependence of viscosity. Unlike isotropic materials, liquid crystals exhibit varying viscosities depending on the orientation of their long-axis director. In the case of cellulose nanocrystals, which are rod-like particles derived from cellulose, their unique shape and anisotropic nature lead to different resistance to flow along different directions, making their viscosity highly directional and dependent on their alignment relative to the flow field. The field of liquid crystals offers an additional perspective on their behavior under shear rates, which was not thoroughly explored in this study [54]. When subjected to shear flow, the velocity of the fluid varies continuously from the bottom plate to the top plate due to the no-slip boundary conditions. This shear flow is opposed by dissipative forces linked to the fluid's shear viscosity. However, since we are dealing with liquid crystals, these forces strongly depend on the orientational order of the particles. The flow direction relative to the molecular alignment and the flow velocity gradient orientation relative to the director also play crucial roles. These three scenarios, represented by three orthogonal director orientations, are commonly known as Mięsowicz viscosities [64]. This was elaborated into the Leslie-Eriksen [65], [66] continuum theory that includes six viscosity coefficients, which were then reduced to five through the work of Parodi and Currie [67]. These, however, remain rather challenging to measure [68]. Furthermore, the author is not aware of any theoretical or experimental attempt to connect the Leslie-Eriksen formalism to nonlinear oscillatory flows. While this was well outside the scope of this thesis, this would be an interesting direction for future fundamental work in the field.

CHAPTER 5

Summary of results

This chapter provides a concise overview of the findings from all the studies conducted in Papers I-VI. Since the main focus of the thesis is to present findings from the combination of rheological techniques, the FT - rheology and rheo - PLI, the results are focused on validation of the used method in different aspects. The results are organized into two categories based on the state of the cellulose nanocrystal (CNC) systems: self-assembling (Papers I, II, V, VI) or non-self-assembling (Papers III, IV, V). This chapter into the interplay between local orientation, surface charge, and attractive or repulsive forces, which dictate the stability of CNC dispersion. The overall potential energy of interaction among rod-like particles is determined by the combined influence of these forces [35], [39]. Consequently, when one force dominates, either self-assembly or aggregation takes place. Lower ionic strengths favor structural ordering, leading to the formation of liquid crystal domains and repulsive glass phases instead of disordered systems. Conversely, at higher concentrations, increased ionic strength results in the formation of non-self-assembling aggregating systems, which subsequently transform into attractive glass structures. The response of the structure to dilution varies between attraction-driven and repulsion-driven structures. When diluted adequately, repulsive glass exhibits

stable dispersions of NCC particles, while attractive glass/gel forms flocs of NCC particles[69]. The phase diagram in Fig.5.1 summarizes which type of CNC system was investigated in particular Papers included in the present thesis.

The summary of rheological analysis is preceded the chemical and morphological results in this chapter.

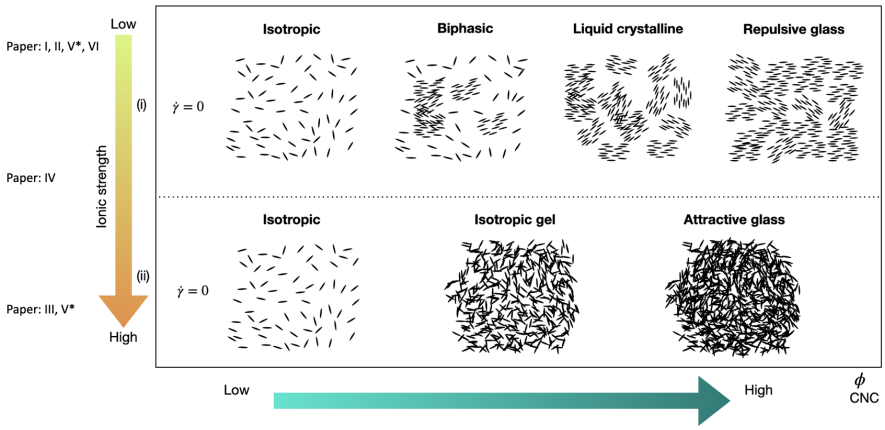

Figure 5.1: The phase diagram of aqueous CNC suspensions was constructed based on CNC concentration and ionic strength, with a focus on differentiating the studies that investigated specific CNC behavior: (i) self-assembling CNC, (ii) non-self-assembling CNC.

5.1 Chemical and morphological characterization

5.1.1 Sulfate content

CNCs with varying sulfate content were prepared as part of this PhD project. In Paper II, the surface charge density, indicating sulfur content, was significantly reduced from 0.81 ± 0.05% to 0.26 ± 0.08% through acid desulfation. The zeta potential of both sulfated and desulfated suspensions exhibited characteristics of a macroscopically stable colloidal suspension. Dynamic Light Scattering (DLS) analysis revealed that sulfated CNCs had a particle size of 62.8 ± 0.2 nm, whereas desulfated CNCs were nearly three times larger, mea-

suring 180.9 ± 9.1 nm. This increase in size was attributed to strong attractive forces prevailing over repulsive interactions. On the other hand, for further exploring the surface charge content on self-assembling and interactions properties CNCs with 3 different sulfate content were prepared in a cooperation with the Westman group at Chalmers. Potentiometric titration has shown that: uCNC had 330 μ mol/g (Paper III), pCNC had 160 μ mol/g (Paper IV) and CNC-$_L$OSO$_3$H: 275 μ mol/g, CNC-^{H}OSO$_3$H: 170 μ mol/g (Paper V). These systems exhibited features characteristic for chemically stable colloidal suspensions, confirmed by zeta potential measurements.

5.1.2 Evaluation of the CNC surface modifications

Synthesis of dialkylamines, dialkylamine azetidinium salts molecules (Open and closed forms) was done for Papers III,IV. To confirm the success of obtained structures, ^{1}H NMR was performed for all the samples and ^{13}C NMR when necessary. The sulfate content, degradation onset temperature and zeta-potential for pristine CNC and modified CNC suspensions for Papers III-V are compiled in Table 1.

In each case, the thermal stability of modified CNC increased considerably. Additionally, replacement of proton with different counterions leads to quite higher thermal stability compare to grafting with azetidinium salts. The increase in degradation onset temperatures of the modified CNC samples confirms the success of the surface modifications. All CNC systems had an average zeta potential close to stable colloidal suspensions [51], [52].

Fig. 5.2 displays the FTIR full range spectra for pCNC and modified CNC samples. All samples exhibit the expected signal indicating the presence of cellulose [70]. The spectra show a broad band between 3600 and 3000 cm^{-1}, corresponding to the –OH groups on cellulose. Additionally, a peak at 3000-2900 cm^{-1} is observed in all samples, which is attributed to the aliphatic C-H bonds on cellulose and the grafted propyl-2-hydroxy-di-alkyl chains (Fig.5.2 (a), (b)). The presence of a peak at 901 cm^{-1} suggests the C-O-C bond between each glucose unit, while the peak at 1640 cm^{-1} corresponds to absorbed water on the cellulose. Furthermore, the peak at 814 cm^{-1} corresponds to the C-O-S bond, indicating the presence of sulfate half-ester and diester [71]. The modified samples exhibit a stronger peak at approximately 2850 cm^{-1}, indicating an increased number of CH_2 groups as expected. Moreover, a slight shift from 814 cm^{-1} to 808 cm^{-1} in the C-O-S region confirms the successful

Table 5.1: Summary CNC chemical characterization data.

Type of CNC	Paper	Sulfate content [μmol/g]	Degradation Onset Temperature [°C]	ζ-potential [mV]
pristine CNC	III	330	145.1	47.0
C_{11}-N-C_1-(...)	III	330	231.2	31.0
C_{11}-N-C_3-(...)	III	330	177.6	30.3
C_{11}-N-C_6-(...)	III	330	218.6	32.1
C_9-N-C_3-(...)	III	330	179.7	30.2
C_{11}-N-$C_{6(2Et)}$-(...)	III	330	179.8	29.8
untreated CNC	IV	160	150	33.2
C_6-N-C_6-(...)	IV	160	263	34
C_9-N-C_3-(...)	IV	160	270	33.4
C_{11}-N-C_1-(...)	IV	160	270	35.8
CNC-$^{H}OSO_3H$	V	275	143.2	47.7
CNC-$^{H}OSO_3Li$	V	275	236	29.4
CNC-$^{H}OSO_3Na$	V	275	196.1	35.8
CNC-$^{H}OSO_3K$	V	275	251.3	39.1
CNC-$^{H}OSO_3$TEtOA	V	275	251	32.8
CNC-$^{H}OSO_3$TEtA	V	275	250.2	33.3
CNC-$_{L}OSO_3H$	V	170	155	30.1
CNC-$_{L}OSO_3Li$	V	170	222.3	34.3
CNC-$_{L}OSO_3Na$	V	170	216.3	39.4
CNC-$_{L}OSO_3K$	V	170	226.7	34.5
CNC-$_{L}OSO_3$TEtOA	V	170	237	37.1
CNC-$_{L}OSO_3$TEtA	V	170	245	33.3

azetidinium modification. On the other hand in comparison to low sulfated CNC samples (Fig.5.2 (c)) , as expected, the intensity of the C-O-S bond signal is more intense in the case of high sulfated CNC samples (Fig.5.2 (d)).

5.1.3 TEM

The TEM analysis in Paper II and Paper VI characterized the morphology of sulfated and desulfated CNC suspensions, providing evidence for the strong interactions between CNC-CNC particles that result in distinct rheological and birefringent properties.

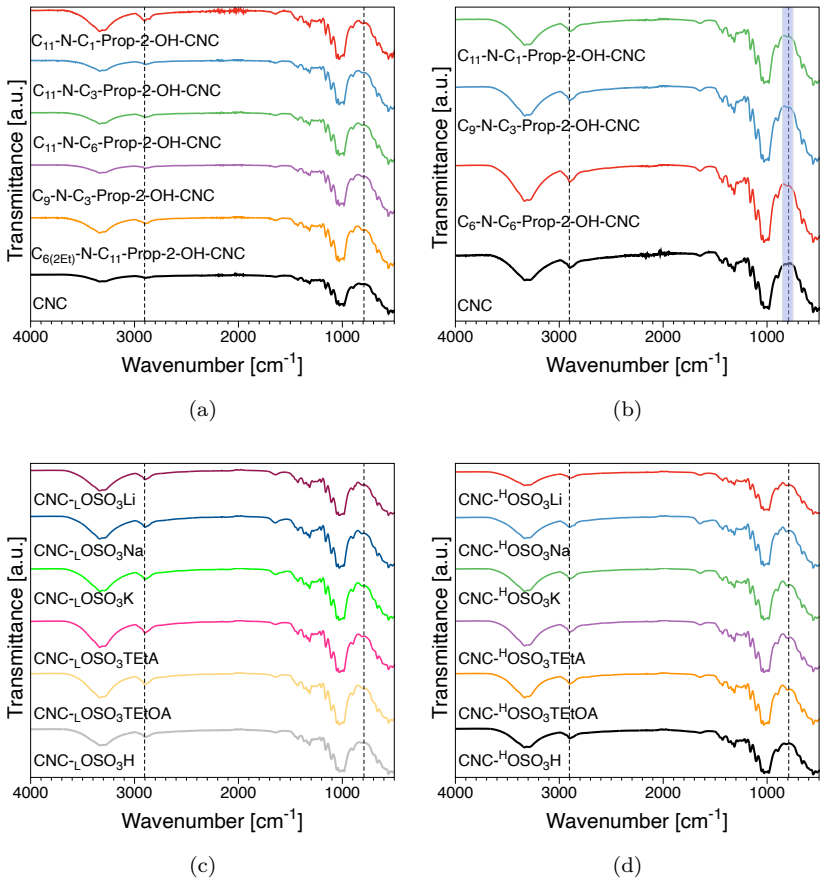

Figure 5.2: Full range FTIR of CNC and surface modified CNC investigated (a) Paper III, (b) Paper IV, (c) - (d) Paper V.

In Paper II, the analysis revealed that at a concentration of 3.9 wt%, a fine network of apparent fibers was observed, while this network was less pronounced for a concentration of $0.77'^{D}$ wt% (Fig. 5.3 (a), (b)). On the other hand, in Paper VI, the morphology of individual particles was examined, depending on the fraction. The grids used for TEM analysis were optimized and prepared following the protocol developed by Parton et al. [72]. Consis-

tent with previous studies, the observation of single bundles leading to chiral self-assembly was made. Notably, there was a significant difference in length among the different fractions, particularly in the case of SR- and LR-CNCs.

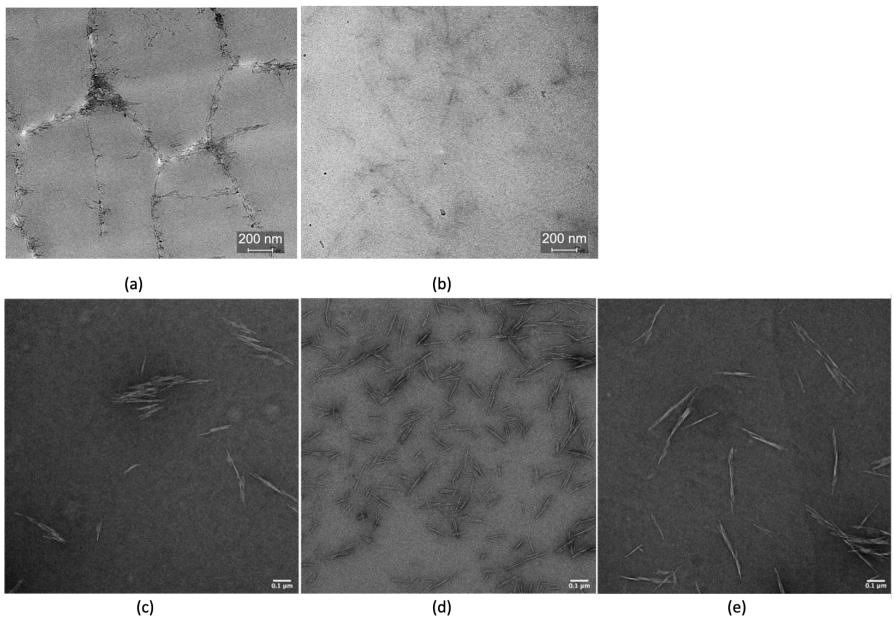

Figure 5.3: Examples of TEM micrographs for self-assembling CNCs systems: Paper II (a) 3.9 wt% CNC, (b) $0.77'^{D}$ wt%, Paper VI 0.0001 wt% (c) I-CNC, (d) SR-CNC, (e) LR-CNC.

5.1.4 The 3D aspect ratio

CNC particles are commonly known to have a rod-like shape. Traditionally, the aspect ratio, which compares the length to the width, has been calculated using AFM measurements. However, in recent years, there has been a growing recognition of the importance of considering the third dimension, the thickness. One significant drawback of employing AFM for morphological analysis of CNCs is the size of the AFM tip, which typically possesses a radius of curvature of approximately 5-10 nm, similar to the width of individual CNCs. Consequently, the profiles of particles in the scanning direction tend to be

smoothed out. Although this effect does not notably impact length measurements, which align with TEM results, the width values obtained from AFM are highly unreliable[73], [74].

Nevertheless, AFM can provide an estimation of the height profile, which can be used to determine the thickness for subsequent calculations. In the case of Paper VI, a combination of AFM and TEM techniques was employed to calculate the 3D aspect ratio. A population of 250 single particles was analyzed. The average lengths were found to be approximately 264 ± 72 nm for the I-CNC, 136 ± 31 nm for the SR-CNC, and 305.6 ± 80 nm for the LR-CNC. Additionally, the equivalent area width (Weq) was determined using a method described by Parton et al. (2022)[72]: Weq^{I} ± 37.9 ± 10 nm, Weq^{SR} ± 20.9 ± 8 nm, and Weq^{LR} ± 31.6 ± 11.1 nm.

By analyzing the AFM data, it was possible to estimate the mean thickness $< T >$, which then enabled the prediction of the 3D aspect ratio using the formula $\alpha_{3D} = L/\sqrt{W_{AE} < T >}$ [72]. The average 3D aspect ratios were found to be 26.6± 10 for the initial CNCs, 20.9± 12.2 for the SR-CNCs, and 35.4± 10.4 for the LR-CNCs. As anticipated, the longest rods exhibited the highest aspect ratios.

5.1.5 POM

The preparation method which affects the rheoological properties was captured on POM images. The 'coarse' microstructures are defined in this PhD project to CNC systems where colors are absent in POMs but bright agglomerates are seen vs. 'fine' microstructures where colors are a continuous field in POMs with no obvious agglomerates (Fig.5.4).

Figure5.5 illustrates examples of polarized optical microscopy (POM) images exhibiting both 'coarse' microstructures (a)-(c) from Paper I and (g), (i) from Paper V, as well as "fine" microstructures from Paper II. As anticipated, the isotropic 2wt% suspension (Fig.5.5 (a)) displays no birefringence. However, at higher concentrations in the "coarse" systems where significant agglomeration occurs, liquid crystalline domains become evident in POM images as optically active regions without specific colors. Notably, the impact of sonication in dispersing these agglomerates is apparent in the suspensions investigated in Paper V, as demonstrated by the example of the 4wt% CNC-$_L$OSO$_3$H suspension (Fig.5.5 (g), (h)).

Conversely, the absence of agglomerates in the "fine" microstructures results

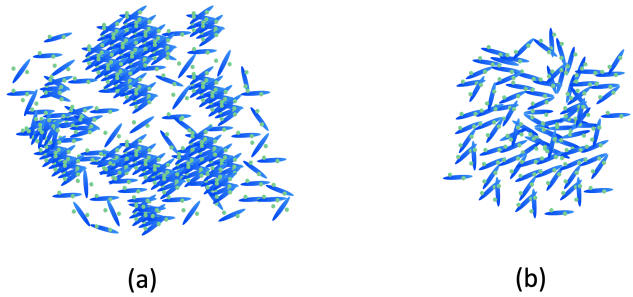

Figure 5.4: Representative interpretation of (a) 'coarse' (b) 'fine' CNC microstructures.

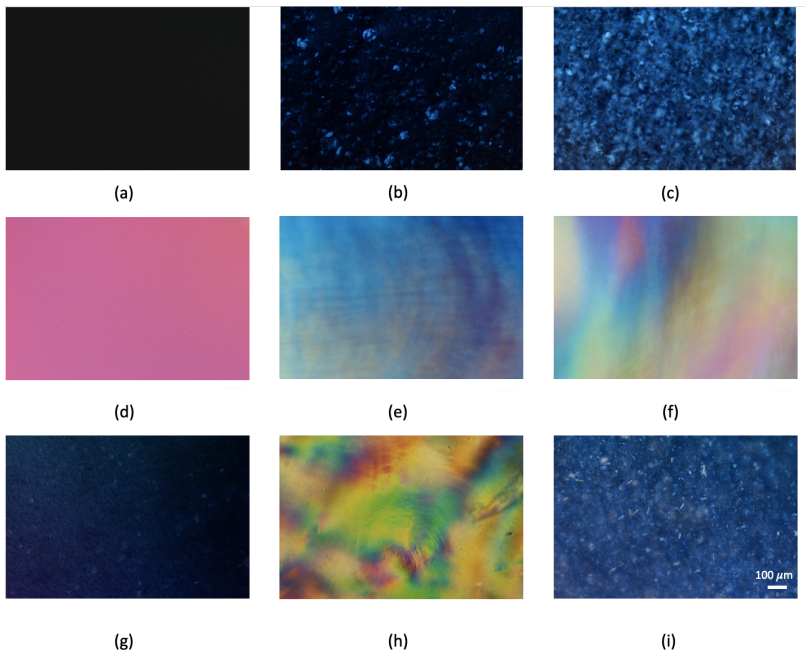

Figure 5.5: Representative micrographs for Paper I: (a) 2 wt% CNC, (b) 4 wt% CNC, (c) 7 wt% CNCs; Paper II: (d) 2 wt% CNC, (e) 3 wt%, (f) 5 wt% sulfated CNCs; Paper V 4 wt%: (g) CNC-$_L$OSO$_3$H nonsonicated, (h) CNC-$_L$OSO$_3$H sonicated, (i) CNC-^{H}OSO$_3$H sonicated.

in POM images showing a continuous distribution of colors in the non-isotropic phase. These images were captured for sulfated CNC suspensions studied in Paper II. Due to the retardation plate, the isotropic phase can be identified as bright pink and oriented (mesophase) regions, as different than pink.

5.2 Rheological characterization

5.2.1 Oscillatory shear

During the investigation of various cellulose nanocrystal (CNC) systems, it was observed that the formation and distribution of a network depended on the applied conditions. Based on these observations, nomenclature notes were proposed from a rheological perspective. In all the publications presented, a parameter known as the "percolation threshold" (ϕ_c) was defined as the minimum concentration at which a CNC suspension exhibits a rheological response dominated by elasticity, indicated by $G' > G''$". We consider a material to have a "gel-like" behavior when $G' \geq G''$". It is worth noting that weakly percolated networks fall under this category, where an increase in the angular frequency (ω) can disrupt the percolated network, resulting in a liquid-like behavior with $G' < G''$". These features were captured by the FT-rheology analysis. On the other hand, the concept of the "gel point" (ϕ_g), as defined by Winter and Chambon[75], refers to the concentration at which the dynamic moduli, $G' \approx G''$ and $G', G'' \sim \omega^{\alpha}$. Therefore, the term "gel" can be associated with isotropic, biphasic, and liquid crystalline phases depending on the preparation of the sample and its surface charge.

5.2.2 Linear viscoelasticity of CNC suspensions

In Paper I, the focus was on investigating CNC suspensions within the range of 2-9 wt%. The amplitude sweeps conducted in this study revealed a general trend: the dynamic moduli values increased with concentration. At the lowest concentration of 2 wt%, the behavior was found to be dependent on the angular frequency, exhibiting characteristics of both a gel-like and a liquid-like substance depending on the applied frequency. However, for all concentrations above 2 wt%, a consistent gel-like behavior was observed.

Paper II focused on studying the impact of surface charge on CNC suspensions. The results demonstrated that desulfation, by the removal of sulfate

groups, led to an increase in the dynamic moduli of the investigated CNC suspensions. It was observed that the percolation threshold for sulfated CNC occurred at a concentration of 5 wt%, whereas for desulfated CNCs, it was significantly lower at 0.73 wt%. The reason behind this observation is that desulfation reduces the surface charge density of CNC, thereby promoting stronger attractive forces between the CNC particles.

Papers III and IV provided evidence that surface modification enhances the interactions between CNC particles and linkers, resulting in higher dynamic moduli overall. Regardless of the specific type of grafted azetidinium salt, a gel-like behavior was observed at approximately 1.5 wt% for the modified CNC suspensions. In contrast, for untreated CNC, the gel-like behavior was detected at a higher concentration of 3 wt%.

Paper V specifically examined CNC suspensions with a concentration of 4 wt%. The study revealed that the particular choice of monovalent counterion as a replacement for the proton did not significantly impact the results. Instead, the surface charge and the method of preparation played a more crucial role. All the suspensions analyzed in this study exhibited a gel-like behavior. However, when comparing CNC-$_L$OSO$_3$H and CNC-^{H}OSO$_3$, it was observed that sonication of samples prior to rheological characterization decreased the overall values of dynamic moduli for CNC-$_L$OSO$_3$H. Conversely, CNC-^{H}OSO$_3$, even when sonicated, exhibited dynamic moduli two orders of magnitude higher than those of non-sonicated CNC-$_L$OSO$_3$H. This discrepancy can be attributed to the higher surface charge of CNC-^{H}OSO$_3$, which enables the dominance of attractive forces over repulsive forces.

The variations in aspect ratio studied in Paper VI revealed that, despite analyzing the same concentrations with identical counterions and surface charges, the percolation threshold favored longer nanorods. This study demonstrated that both I-CNC and LR-CNC exhibited a gel-like behavior at concentrations below 4 wt%, whereas SR-CNC required concentrations above 4 wt% to exhibit a similar gel-like behavior.

The graph in Fig. 5.6 illustrates the storage and loss modulus (G', G'') of CNC suspensions, obtained through dynamic strain sweep measurements, with angular frequencies of $\omega = 0.6$ rad/s.

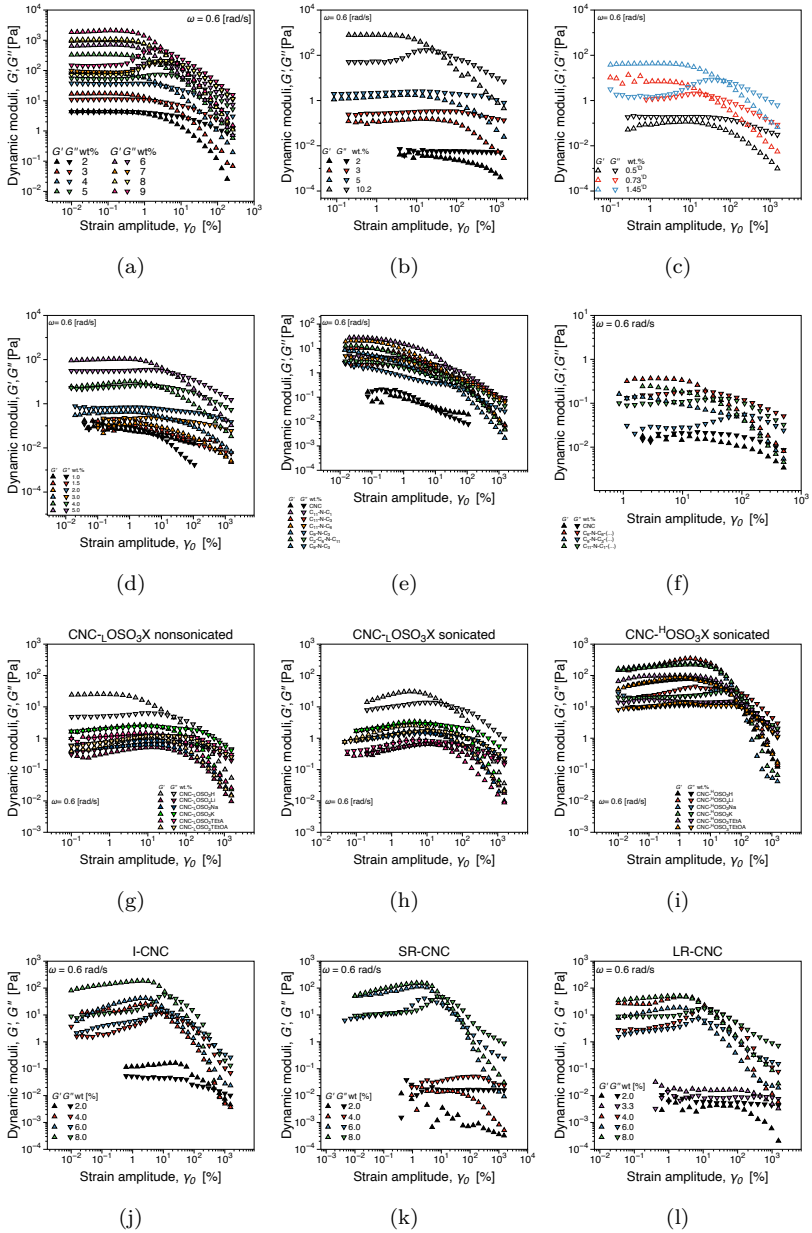

Figure 5.6: Linear viscoelastic properties of CNC for all investigated CNCs systems from strain sweep measurements at $\omega = 0.6$ rad/s: (a) Paper I, (b) - (c) Paper II, (d) - (e) Paper III, (f) Paper IV, (g) - (i) Paper V, (j) - (l) Paper VI.

5.2.1.1 Nonlinear oscillatory shear analysis

5.2.1.1.1 Fourier-transform rheology

Fig.5.7 shows the graphical summary of all investigated CNC suspensions as the nonlinear material response as expressed by the third relative higher harmonic, $I_{3/1}$. The aim of this thesis was to investigated if it is possible to detect characteristic features at transitions, such as percolation, gelation or phase transition. Due to many investigated different systems it was possible to detect these features at the critical concentrations. Similarities were observed at these changes independently on the nature of studied material. The main nonlinear material response characteristics primarily of focus are those that do not obey theoretical scaling predictions in the MAOS region. For $I_{3/1}$, this includes non-quadratic scaling with the strain amplitude, $I_{3/1} \propto \gamma_0^n, n \neq 2$, γ_0 dependence in the form of multiple scaling regions ($n = f(\gamma)$) and ω-dependence in nonlinear scaling ($n = f(\omega)$), all collectively dubbed nonlinear 'oddities'. Based on the data from strain sweep and frequency sweep experiments, it was observed that as concentrations approached the percolation threshold, there was an observable dependence on angular frequency (ω) and the presence of multiple scaling regions. With further increases in concentration and/or surface charge, similar multiple scaling regions were observed, but with reduced dependence on ω. Frequency sweep measurements confirmed that these samples were at the rheological gel point, indicating the formation of a strong CNC network with sufficiently high connection points between nanoparticles, making it resistant to disruption. The distinct regions between particular samples differed, however there were always $n < 2$. Continued increases in concentration and surface charge resulted in the least ω-dependence, characterized by a distinct 'plateau' region. This plateau region indicated the existence of a resilient internal network gel. It was also associated with the presence of 'coarse' structures, which were a result of the specific preparation method. In Paper I, for instance, suspensions were stirred using a table shaker. Combining this additional step with the third relative higher harmonic analysis and the absence of color in polarized optical microscopy (POM) analysis, it can be inferred that these 'coarse' systems contained significant amounts of agglomerates. The presence of an additional step, such as the application of γ_0 (shear strain), suggested the disruption of agglomerates. However, this distinctive 'plateau' region was not observed in lower concentrations, systems

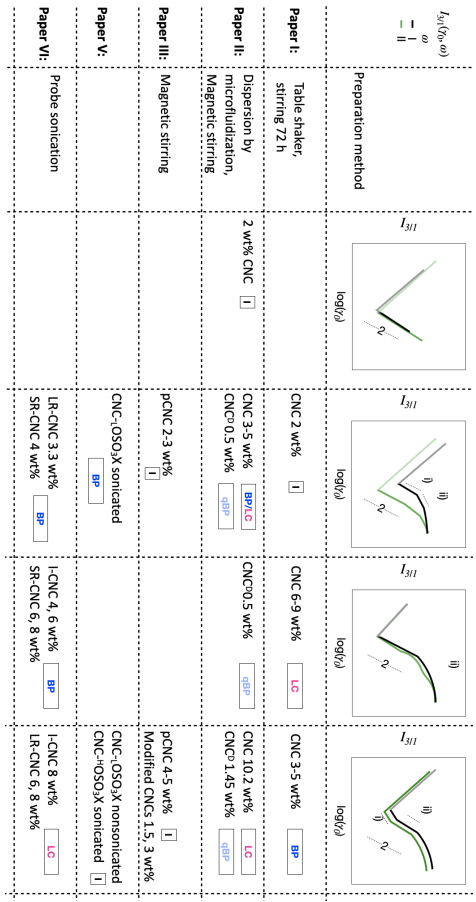

Figure 5.7: Graphical summary of phase behavior as estimated based on all investigated CNC systems which differed in surface charge, counterions, concentrations and aspect ratio from the third relative higher harmonic $I_{3/1}$.

with lower surface charge, or suspensions prepared using a magnetic stirrer or sonication.

5.2.1.1.2 Stress decomposition

Furthermore, the stress decomposition analysis revealed similarities among different transitions. The stress decomposition analysis involved the characterization of dimensionless ratios, specifically strain-stiffening (S) and shear-thickening (T). Based on a comprehensive analysis of the data, three distinct types of behavior were identified, which could be attributed to either phase transitions or percolation/gelation transitions, presented in Fig.5.8.

For suspensions with the lowest concentrations below the rheological gel point, a characteristic nonlinear intra-cycle strain-stiffening behavior was observed, where $S > 0$, alongside intra-cycle shear-thinning ($T < 0$). Regardless of the concentration, phase, counterion, or aspect ratio, all suspensions exhibited intra-cycle strain-stiffening ($S > 0$). The distinguishing factor among higher concentrations was the occurrence of local intra-cycle shear-thickening behavior, where $T > 0$. Upon analyzing all the studies, it can be concluded that the local shear-thickening behavior in T corresponds roughly to the onset of the viscous-like behavior in G'', and appears to be a more sensitive parameter in certain cases for indicating jamming/yielding during strain sweeps.

The third case, observed in the materials characterized in Paper I and II, displayed not only local shear-thickening that transitioned to shear-thinning, but also local strain-softening where $S < 0$. The presence of this feature could be attributed to significant differences at the microstructural level, as observed through polarized optical microscopy (POM), such as distinguishing between 'coarse' and 'fine' structures. The occurrence of local strain-softening may be associated with the dynamics of agglomerates within the 'coarse' microstructure described in Paper I, which resulted from the specific preparation method. In the case of the 10.2 wt% suspension (Paper II), the presence of the same feature may indicate the formation of the strongest network. Interestingly, this concentration exhibited color fading in POM analysis, further supporting the hypothesis regarding the presence of 'coarse' structures.

Based on all above, the preparation method significantly influences the rheological behavior of CNC (cellulose nanocrystal) suspensions. When the suspensions are prepared by dispersing with a table shaker, certain observations indicate the presence of agglomerates: the presence of a 'plateau' in the $I_{3/1}$ parameter, local strain-softening ($S < 0$), and the absence of colors on POM. Consequently, these suspensions possess a 'coarse' microstructure. On the other hand, CNC suspensions prepared using a sonication probe and/or long

magnetic stirring display a colorful pattern on POM, suggesting a more homogenized structure, which can be described as 'fine'. This 'fine' structure comprises smaller LC (liquid crystal) domains that are more susceptible to disruption when subjected to strain.

5.2.2 The steady shear characterization

All factors mentioned at the beginning of this chapter has impact also on the steady shear viscosity. The steady shear measurements were performed for CNC systems presented in Papers I, II, IV, V and VI. Generally, steady shear viscosity functions can be categorized into three groups:(a) Suspensions with a Newtonian plateau exhibiting a zero-shear viscosity, followed by a shear-thinning region. This behavior is typically observed at low, isotropic concentrations. (b) Shear viscosity functions displaying three-regions with varying slopes. Depending on the study on the study, this region is classified as biphasic[76], liquid-crystalline[77]–[80], or a combination of both[81]. (c) Single shear-thinning region, which is characteristic of high concentrations nearing either the attractive or repulsive glass state. Graphical representations of steady shear viscosities is presented in Fig.5.9

In the investigated CNC materials for this thesis, the following viscosity patterns were observed:

A characteristic Newtonian plateau followed by a shear-thinning region was observed at 2 wt% CNCs and 0.5, 0.73 wt% CNC^D (Paper I, II), as well as at 2 and 4 wt% CNCs and 6 wt% SR-CNC (Paper VI). The three-region shear viscosity pattern was observed at concentrations ranging from 3 to 9 wt% (Paper I), and at 3 and 5 wt% (Paper II). Additionally, it was observed for non-sonicated and sonicated samples of 4 wt% CNC-$_L$$OSO_3X$ (Paper V) and at 6 and 8 wt% for I-CNC, LR-CNC, and 8 wt% SR-CNC (Paper VI). On the other hand, shear-thinning behavior was observed at 10.2 wt% CNC, 1.45 wt% CNC^D (Paper II), and 4 wt% sonicated CNC-^{H}OSO^3X (Paper V).

In Paper IV, the behavior of 1.5 wt% CNC suspensions was found to be inconclusive. Despite the fact that untreated CNC exhibited the characteristic viscosity behavior expected for isotropic systems, it displayed a colorful pattern during rheo-PLI analysis. On the other hand, the modified CNC suspensions, although exhibiting two to three different slopes, did not show birefringent properties, except for the case of one grafted linker onto the CNC surface (C_{C11}-N-C_1-Prop-2-OH-CNC).

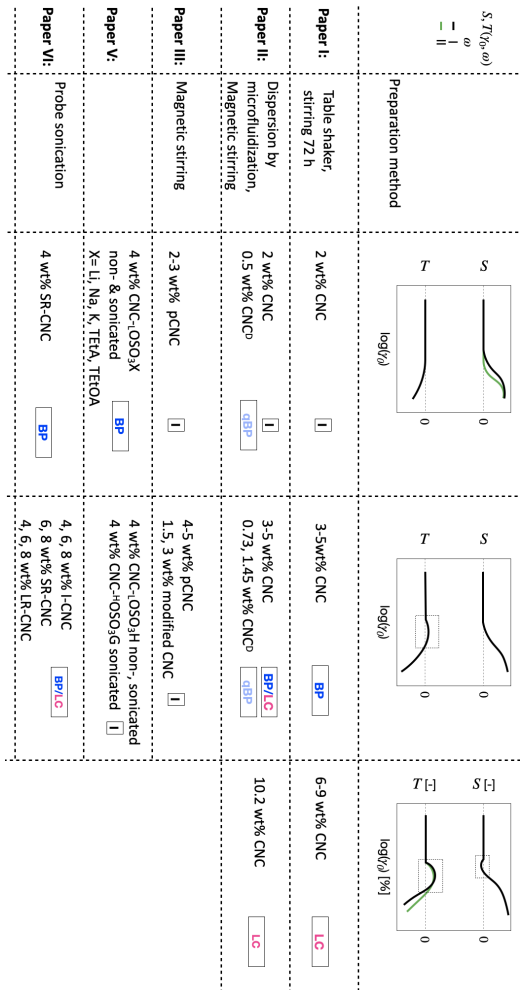

Figure 5.8: Graphical summary of phase behavior as estimated based on all investigated CNC systems which differed in surface charge, counterions, concentrations and aspect ratio from the stress decomposition analysis represented by S, T nonlinear parameters.

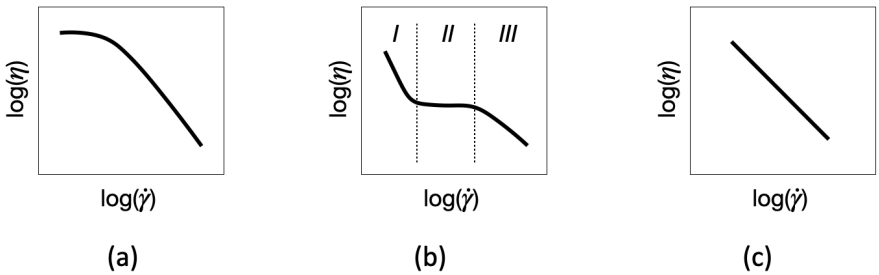

Figure 5.9: Graphical representation the steady shear viscosity behavior depending on the phase and concentration of CNC suspensions.

5.2.2.1 Rheo-PLI

Furthermore, the evolution of CNC suspensions flow while applying shear rate was recorded during steady shear measurements, which can be represented as still-frames captured at different $\dot{\gamma}$. Fig.5.10,5.11 represent examples of this vizualization for all investigated CNC suspensions without applying $\dot{\gamma}$ and at maximum value, $\dot{\gamma}$= 100 [1/s]. From the self-assembling category of studied CNC materials, the lowest, isotropic concentrations didn't exhibit birefringent properties. However, the Maltese-cross pattern indicating a parallel orientation of one of the main axes of the optical indicatrices of a birefringent material, which is CNC, in the plane of polarization of the incident light was observed at the highest applied shear rate. This feature was observed at 2-4 wt% (Paper I), 0.73, 1.45 wt% CNC^D (Paper II), 1.5 wt% uCNC, C_{11}-N-C_1-Prop-2-OH-CNC (Paper IV), 4 wt% SR-CNC (Paper VI). Then, as the fraction of the liquid crystal phase increased, a colorful pattern was observed both as large isochromatic areas at the beginning of the tests and in the Maltese-cross patterns. It was observed at 5-9 wt% (Paper I), 3, 5, 10.2 wt% (Paper II), 4 wt% CNC-$_L$$OSO_3X$ sonicated (Paper V) and 4, 6, 8 I-CNC, 6, 8 wt% SR-CNC, 3.3, 4, 6, 8 wt% LR-CNC (Paper VI).

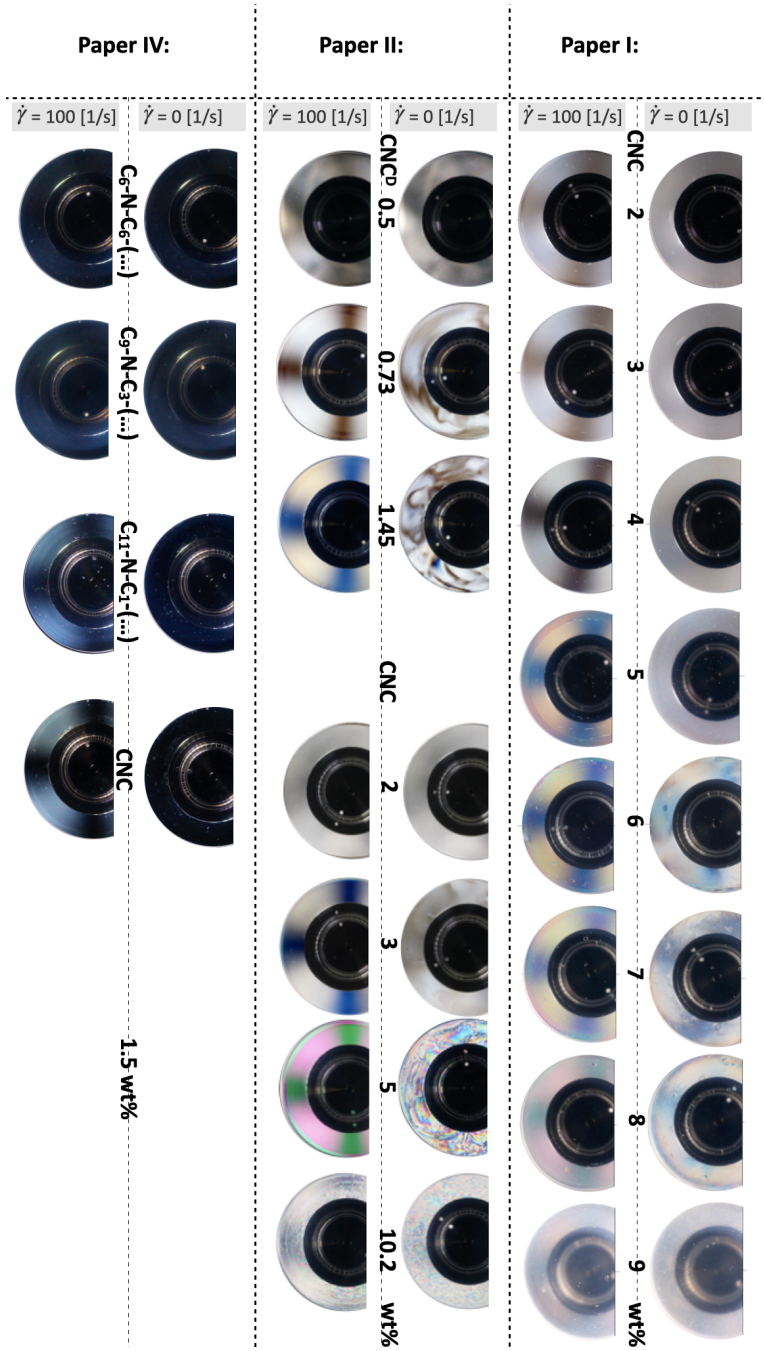

Figure 5.10: Examples of still-frames captures at $\dot{\gamma}$=0 and $\dot{\gamma}$=100 [1/s] for CNC suspensions investigated in Paper I, II, IV.

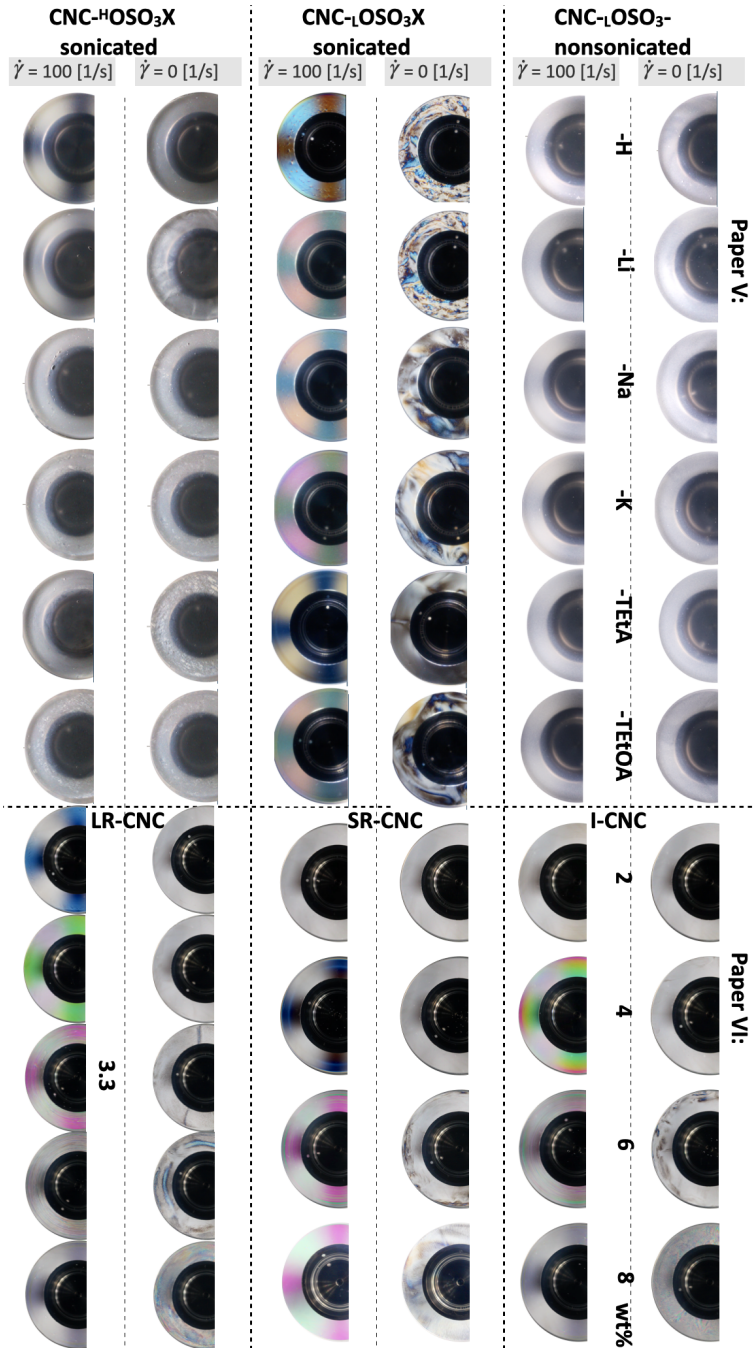

Figure 5.11: Examples of still-frames captures at $\dot{\gamma}$=0 and $\dot{\gamma}$=100 [1/s] for CNC suspensions investigated in Paper V, VI.

CHAPTER 6

Conclusions. Current and future work

While the existence of CNC particles has been known since the mid-20th century, there still exists a knowledge gap regarding the understanding of the rheological properties of CNC suspensions and how they are connected to the structural evolution at all involved lengthscales in such systems. These suspensions can be categorized into self-assembling and non-self-assembling systems, depending on factors such as ionic strength, salt, temperature, ultrasound energy, and concentration. To better observe changes in microstructure during rheological measurements, it is crucial to employ highly sensitive techniques and consider the use of multiple methods to enhance our understanding of phase transitions. Nonlinear oscillatory shear and rheo-PLI are proposed as potential tools for detailed rheological analysis of CNC systems, capable of capturing characteristic features at critical concentrations during phase transitions, percolation, or gel point. These features cannot be adequately captured by conventional rheological analysis.

Based on all studies above, it can be concluded that the onset of the Maltese-cross birefringence pattern, signals the domains orientation in the flow direction. For the isotropic phase domains will refer to the CNCs particles and boundaries at mesogens in the liquid crystalline phase. In turn, the structural

changes in mesogens, can be detected by the rheological characterization. Applying shear rate causes a multiscale orientation of CNCs particles in aqueous systems. That has a significant impact on the resulting viscosity and colorful pattern. It would be beneficial to investigate it by applying rheo-PLI-SAXS technique, which is more sensitive.

The stability of CNC suspensions is determined by the combined influence of various forces acting on the colloidal particles. The DLVO - and non - DLVO - interactions provide explanations for their stability. The DLVO theory considers the interplay between van der Waals and Coulombic electrostatic forces, while the non - DLVO forces take into account the charge, distribution, and spatial dimensions of ions. The dominance of a particular force will lead to self-assembly or aggregation. In this thesis, two different cellulose nanocrystal systems were extensively analyzed using nonlinear rheological techniques and/or rheo-PLI.

Cellulose nanocrystals with lower sulfate content and Na^+ cations undergo self-assembly, transitioning from an isotropic phase to biphasic and liquid crystalline phases as the CNC concentration increases. The identification of these phases was achieved through combined analysis using optical microscopy, linear viscoelastic oscillatory shear, steady shear viscosity functions, and rheo-PLI experiments. The results were further compared with FT-rheology and stress decomposition analyses to understand the influence of the specific CNC phase on nonlinear material parameters. This analysis revealed microstructural changes that were not observable through linear viscoelastic measurements, while the macroscopic PLI data detected organized CNCs floating in a polydomain structure.

On the other hand, cellulose nanocrystals with higher sulfate content and $-OSO_3^-$ groups attached to protons do not exhibit self-assembly. Instead, due to their dominant attractive nature, they agglomerate into isotropic gels and attractive glass phases as the concentration increases. The evolution of nonlinear rheological behavior was investigated through FT-rheology and stress decomposition analyses. Analysis of Papers III and IV indicates that surface modification of CNCs by functionalizing the sulfate groups with dialkylamines significantly enhances their thermal stability and dynamic moduli.

Ionic strength has a significant impact on the rheological properties of CNC suspensions. Some suspensions exhibit organization and birefringence properties, while others undergo agglomeration with increasing concentration. Ad-

ditionally, depending on the ionic strength, aqueous CNC suspensions with the same concentrations show different changes in microstructure. A distinct nonlinear material response, characterized by a third relative higher harmonic, $I_{3/1}$, was observed only for isotropic gels. This feature presented as an intermediate 'plateau' in the MAOS region, representing a constant nonlinear output ($I_{3/1} \propto \gamma_0^n$, with $n \approx 0$). This behavior became more pronounced with increasing strain amplitude and concentration. When comparing suspensions with the same concentrations from different CNC systems, a local decrease in the S parameter at intermediate strain amplitude was observed only for self-assembling CNC. This behavior could be associated with the presence of liquid crystalline domains.

The choice of preparation method significantly influences both the self-assembly of CNC into liquid crystalline structures and the resulting rheological properties. Utilizing a probe sonicator to disperse CNCs aids in the breakdown of agglomerates that hinder the self-assembling properties of CNCs.

In terms of monovalent counterions, the study revealed no significant differences in the optical and rheological properties among specific ions. This finding suggests the possibility of exploring this field further by investigating the impact of divalent counterions.

Additionally, it would be beneficial to investigate the effect of different sources of CNC. While this PhD project focused on CNCs produced through acidic hydrolysis, there has been no examination of enzymatic or bacterial CNCs in terms of nonlinear rheological characterization. Exploring these alternative sources would provide valuable insights into their rheological behavior.

References

[1] A. Dufresne, "Cellulose nanomaterials and polymer nanocomposites," *Annual Transactions of the Nordic Rheology Society*, vol. 27, pp. 3–9, 2019.

[2] R. J. Moon, C. R. Frihart, and T. Wegner, "Nanotechnology applications in the forest products industry," *Forest products journal*, vol. 56, no. 5, pp. 4–10, 2006.

[3] H. Tao, N. Lavoine, F. Jiang, J. Tang, and N. Lin, "Reducing end modification on cellulose nanocrystals: Strategy, characterization, applications and challenges," *Nanoscale Horizons*, vol. 5, no. 4, pp. 607–627, 2020.

[4] M. Hubbe, A. Ferrer, P. Tyagi, *et al.*, "Nanocellulose in thin films, coatings, and plies for packaging applications: A review," *BioResources*, vol. 12, 2017.

[5] Z. Bazrafshan, "Multi-functional coating of polymeric spherulites for chiral photonic cellulose nanocrystal films," *Cellulose*, vol. 27, no. 17, pp. 6235–6247, 2020.

[6] M.-C. Li, Q. Wu, K. Song, S. Lee, Y. Qing, and Y. Wu, "Cellulose nanoparticles: Structure–morphology–rheology relationships," *ACS Sustainable Chemistry & Engineering*, vol. 3, no. 3, pp. 821–832, 2015.

[7] A. Dufresne, "Nanocellulose: A new ageless bionanomaterial," *Materials Today*, vol. 16, no. 6, pp. 220–227, 2013.

[8] T. Yuan, H. Xie, H. Du, X. Yang, and C. Si, "Recent strategies in preparation of cellulose nanocrystals and cellulose nanofibrils derived from raw cellulose materials," *International Journal of Polymer Science*, vol. 2018, pp. 1–25, 2018.

[9] R. A. Young and R. M. Rowell, "Cellulose structure modification and hydrolysis," *Journal of Polymer Science: Polymer Letters Edition*, vol. 25, pp. 139–140, 1987.

[10] D. Trache, M. H. Hussin, C. T. Hui Chuin, *et al.*, "Microcrystalline cellulose: Isolation, characterization and bio-composites application—a review," *International Journal of Biological Macromolecules*, vol. 93, pp. 789–804, 2016.

[11] "Land area covered by forests in 2019," *http://ec.europa.eu/eurostat/statistics-explained*, (accessed: 21.04.2021).

[12] K. Étienne, "Thermal analysis in the cellulose, paper and textile industry," *Thermochimica Acta*, vol. 110, pp. 471–475, 1987.

[13] R. M. Cherian, A. Tharayil, R. T. Varghese, *et al.*, "A review on the emerging applications of nano-cellulose as advanced coatings," *Carbohydrate Polymers*, vol. 282, p. 119 123, 2022.

[14] D. Trache, A. F. Tarchoun, M. Derradji, *et al.*, "Nanocellulose: From fundamentals to advanced applications," *Frontiers in Chemistry*, vol. 8, 2020.

[15] K. Susheel, D. Alain, M. C. Bibin, *et al.*, "Cellulose-based bio- and nanocomposites: A review," *International Journal of Polymer Science*, vol. 2011, no. 17, pp. 1–35, 2011.

[16] Y. Habibi, L. A. Lucia, and O. J. Rojas, "Cellulose nanocrystals: Chemistry, self-assembly, and applications," *Chemical Reviews*, vol. 110, no. 6, pp. 3479–3500, Jun. 2010.

[17] J.-L. Wertz, J. P. Mercier, and O. Bédué, "Cellulose science and technology," *EPFL Press*, 2010.

[18] A. F. Tarchoun, D. Trache, T. M. Klapötke, M. Derradji, and W. Bessa, "Ecofriendly isolation and characterization of microcrystalline cellulose from giant reed using various acidic media," *Cellulose*, vol. 26, pp. 7635–7651, 2019.

[19] Y. Fumihiro, T. Naoto, and W. Kunihiko, "Research progress in production of bacterial cellulose by aeration and agitation culture and its application as a new industrial material," *Bioscience, Biotechnology, and Biochemistry*, vol. 61, pp. 219–224, 2 1997.

[20] M. Iguchi, S. Yamanaka, and A. Budhiono, "Bacterial cellulose—a masterpiece of nature's arts," *Journal of Materials Science*, vol. 35, no. 2, pp. 261–270, 2000.

[21] H. A. Krässig, *Cellulose : structure, accessibility, and reactivity* (Polymer monographs: 11). Gordon and Breach Science, 1993, ISBN: 2-88124-798-9.

[22] S. Naz, J. S. Ali, and M. Zia, "Nanocellulose isolation characterization and applications: A journey from non-remedial to biomedical claims," *Bio-Design and Manufacturing*, vol. 2, no. 3, pp. 187–212, 2019.

[23] A. Mtibe, T. H. Mokhothu, M. J. John, T. C. Mokhena, M. J. Mochane, and C. Mustansar Hussain, "Chapter 8 - fabrication and characterization of various engineered nanomaterials," in *Handbook of Nanomaterials for Industrial Applications*. 2018, pp. 151–171, ISBN: 978-0-12-813351-4.

[24] M. N. Anglès and A. Dufresne, "Plasticized starch/tunicin whiskers nanocomposite materials. 2. mechanical behavior," *Macromolecules*, vol. 34, no. 9, pp. 2921–2931, Apr. 2001.

[25] A. Mtibe, L. Z. Linganiso, A. P. Mathew, K. Oksman, M. J. John, and R. D. Anandjiwala, "A comparative study on properties of micro and nanopapers produced from cellulose and cellulose nanofibres," *Carbohydrate Polymers*, vol. 118, pp. 1–8, 2015.

[26] T. C. Mokhena and A. S. Luyt, "Investigation of polyethylene/sisal whiskers nanocomposites prepared under different conditions," *Polymer Composites*, vol. 35, no. 11, pp. 2221–2233, 2020/05/11 2014.

[27] B. Medronho, A. Romano, M. G. Miguel, L. Stigsson, and B. Lindman, "Rationalizing cellulose (in)solubility: Reviewing basic physicochemical aspects and role of hydrophobic interactions," *Cellulose*, vol. 19, no. 3, pp. 581–587, 2012.

[28] A. W. T. King, V. Mäkelä, S. A. Kedzior, *et al.*, "Liquid-state nmr analysis of nanocelluloses," *Biomacromolecules*, vol. 19, no. 7, pp. 2708–2720, 2018.

[29] D. Klemm, F. Kramer, S. Moritz, *et al.*, "Nanocelluloses: A new family of nature-based materials," *Angewandte Chemie International Edition*, vol. 50, no. 24, pp. 5438–5466, 2011.

[30] R. J. Moon, A. Martini, J. Nairn, J. Simonsen, and J. Youngblood, "Cellulose nanomaterials review: Structure, properties and nanocomposites," *Chemical Society Reviews*, vol. 40, no. 7, pp. 3941–3994, 2011.

[31] S. Chattopadhyay, H. Keul, and M. Moeller, "Functional polymers bearing reactive azetidinium groups: Synthesis and characterization," *Macromol. Chem. Phys.*, vol. 213, no. 5, pp. 500–512, 2020/05/18 2012.

[32] B. Drouillat, K. Wright, O. David, and F. Couty, "Insight into the regioselectivity of nucleophilic ring-opening of azetidinium ions containing quaternary carbon atoms," *European Journal of Organic Chemistry*, vol. 2012, no. 30, pp. 6005–6012, 2012.

[33] M. Börjesson, K. Sahlin, D. Bernin, and G. Westman, "Increased thermal stability of nanocellulose composites by functionalization of the sulfate groups on cellulose nanocrystals with azetidinium ions," *Journal of Applied Polymer Science*, vol. 135, no. 10, p. 45 963, 2018.

[34] J. Zhang and H. Zeng, "Intermolecular and surface interactions in engineering processes," *Engineering*, vol. 7, no. 1, pp. 63–83, 2021.

[35] D. Horinek, "Dlvo theory," in Springer New York, 2014.

[36] A. Dufresne, *Nanocellulose From Nature to High Performance Tailored Materials*. De Gruyter, 2017.

[37] H. J. Dyson, P. E. Wright, and H. A. Scheraga, "The role of hydrophobic interactions in initiation and propagation of protein folding," *Proceedings of the National Academy of Sciences*, vol. 103, no. 35, pp. 13 057–13 061, 2006.

[38] S. L. J. Thomä, S. W. Krauss, M. Eckardt, P. Chater, and M. Zobel, "Atomic insight into hydration shells around facetted nanoparticles," *Nature Communications*, vol. 10, no. 1, p. 995, 2019.

[39] C. A. Silvera Batista, R. G. Larson, and N. A. Kotov, "Nonadditivity of nanoparticle interactions," *Science*, vol. 6257, 2015.

[40] A. Tiffany and C. Emily D., "Handbook of green materialsy," in 2014, vol. 37, ch. Chiral Nematic Self-Assembly of Cellulose Nanocrystals in Suspensions and Solid Films, pp. 37–56.

[41] Y. Xu, A. Atrens, and J. R. Stokes, "A review of nanocrystalline cellulose suspensions: Rheology, liquid crystal ordering and colloidal phase behaviour," *Advances in Colloid and Interface Science*, vol. 275, p. 102 076, 2020.

[42] A. Douplik, G. Saiko, I. Schelkanova, and V. Tuchin, "Woodhead publishing series in electronic and optical materials," in *Lasers for Medical Applications*. 2013, pp. 47–109.

[43] M. A. C. Mhd Haniffa, Y. C. Ching, L. C. Abdullah, S. C. Poh, and C. H. Chuah, "Review of bionanocomposite coating films and their applications," *Polymers*, vol. 8, no. 7, 2016.

[44] S. N. Fernandes, P. L. Almeida, N. Monge, *et al.*, "Mind the microgap in iridescent cellulose nanocrystal films," *Advanced Materials*, vol. 29, no. 2, p. 1 603 560, 2017.

[45] S. L. Navarro, K. Nakayama, A. Idström, L. Evenäs, A. Ström, and T. Nypelö, "The effect of sulfate half-ester groups on cellulose nanocrystal periodate oxidation," *Cellulose*, Manuscript in review, 2021.

[46] M. Fazilati, S. Ingelsten, S. Wojno, T. Nypelö, and R. Kádár, "Thixotropy of cellulose nanocrystal suspensions," *Journal of Rheology*, Manuscript in review, 2021.

[47] T. Abitbol, A. Palermo, J. M. Moran-Mirabal, and E. D. Cranston, "Fluorescent labeling and characterization of cellulose nanocrystals with varying charge contents," *Biomacromolecules*, vol. 14, no. 9, pp. 3278–3284, 2013.

[48] S. Beck and J. Bouchard, "Auto-catalyzed acidic desulfation of cellulose nanocrystals," *Nordic Pulp & Paper Research Journal*, vol. 29, no. 1, pp. 6–14, 2014.

[49] C. Honorato-Rios and J. P. F. Lagerwall, "Interrogating helical nanorod self-assembly with fractionated cellulose nanocrystal suspensions," *Communications Materials*, vol. 1, no. 1, p. 69, 2020.

[50] M. Hasani, E. D. Cranston, G. Westman, and D. G. Gray, "Cationic surface functionalization of cellulose nanocrystals," *Soft Matter*, vol. 4, pp. 2238–2244, 11 2008.

[51] W. Qi, H.-N. Xu, and L. Zhang, "The aggregation behavior of cellulose micro/nanoparticles in aqueous media," *RSC Adv*, vol. 15, pp. 8770–8777, 12 2005.

[52] M. S. Reid, M. Villalobos, and E. D. Cranston, "Benchmarking cellulose nanocrystals: From the laboratory to industrial production," *Langmuir*, vol. 33, no. 7, pp. 1583–1598, 2017.

[53] X. M. Dong, J.-F. Revol, and D. G. Gray, "Effect of microcrystallite preparation conditions on the formation of colloid crystals of cellulose," *Cellulose*, vol. 5, no. 1, pp. 19–32, 1998.

[54] J. P. F. Lagerwall and G. Scalia, "Liquid crystals with nano and microparticles," in WORLD SCIENTIFIC, 2016, ch. A phenomenological introduction to liquid crystals and colloids, pp. 11–93.

[55] K. Walters and R. I. Tanner, *Rheology: An Historical Perspective.* Elsevier Science, 1998, vol. 7.

[56] B. Howard A., H. John F., and W. Kenneth, "An introduction to rheology," 1989.

[57] J. D. Ferry, *Viscoelastic properties of polymers.* John Wiley & sons, inc., 1980.

[58] K. Hyun and W. Kim, "A new non-linear parameter q from ft-rheology under nonlinear dynamic oscillatory shear for polymer melts system," *Korea Australia Rheology Journal*, vol. 23, no. 4, pp. 227–235, 2011.

[59] K. Hyun, M. Wilhelm, C. O. Klein, *et al.*, "A review of nonlinear oscillatory shear tests: Analysis and application of large amplitude oscillatory shear (laos)," *Progress in Polymer Science*, vol. 36, no. 12, pp. 1697–1753, 2011.

[60] M. Kempf, D. Ahirwal, M. Cziep, and M. Wilhelm, "Synthesis and linear and nonlinear melt rheology of well-defined comb architectures of ps and ppms with a low and controlled degree of long-chain branching," *Macromolecules*, vol. 14, 2013.

[61] K. Hyun and W. Kim, "A new non-linear parameter q from ft-rheology under nonlinear dynamic oscillatory shear for polymer melts system," *Korea-Australia Rheology Journal*, vol. 23, no. 4, pp. 227–235, 2011.

[62] R. Ewoldt, A. Hosoi, and G. McKinley, "New measures for characterizing nonlinear viscoelasticity in large amplitude oscillatory shear," *Journal of Rheology*, vol. 52, no. 6, pp. 1427–1458, 2008.

[63] R. Kádár, M. Fazilati, and T. Nypelö, "Unexpected microphase transitions in flow towards nematic order of cellulose nanocrystals," *Cellulose*, vol. 27, no. 4, pp. 2003–2014, 2020.

[64] M. Mięsowicz, "The three coefficients of viscosity of anisotropic liquids," *Nature*, vol. 158, no. 4001, pp. 27–27, 1946.

[65] J. L. Ericksen, "Conservation laws for liquid crystals," *Transactions of The Society of Rheology*, vol. 5, no. 1, pp. 23–34, 1961.

[66] F. M. Leslie, "Some constitutive equations for liquid crystals," *Archive for Rational Mechanics and Analysis*, vol. 28, no. 4, pp. 265–283, 1968.

[67] G. J. O'neill, "The determination of the viscosity coefficients of nematic liquid crystals," *Liquid Crystals*, vol. 1, no. 3, pp. 271–280, 1986.

[68] R. Orr and R. A. Pethrick, "Viscosity coefficients of nematic liquid crystals: I. oscillating plate viscometer measurements and rotational viscosity measurements: K15†," *Liquid Crystals*, vol. 38, no. 9, pp. 1169–1181, 2011.

[69] M. Nordenström, A. Fall, G. Nyström, and L. Wågberg, "Formation of colloidal nanocellulose glasses and gels," *Langmuir*, vol. 33, no. 38, pp. 9772–9780, 2017.

[70] D. E. Ciolacu, F. Ciolacu, and V. I. Popa, "Amorphous cellulose - structure and characterization," *Cellulose chemistry and technology*, no. 45, pp. 13–21, 2011.

[71] G. Chen, B. Zhang, J. Zhao, and H. Chen, "Improved process for the production of cellulose sulfate using sulfuric acid/ethanol solution.," *Carbohydrate polymers*, vol. 95 1, pp. 332–7, 2013.

[72] T. G. Parton, R. M. Parker, G. T. van de Kerkhof, *et al.*, "Chiral self-assembly of cellulose nanocrystals is driven by crystallite bundles," *Nature Communications*, vol. 13, no. 1, p. 2657, 2022.

[73] Y. Boluk, R. Lahiji, L. Zhao, and M. T. McDermott, "Suspension viscosities and shape parameter of cellulose nanocrystals (cnc)," *Colloids and Surfaces A: Physicochemical and Engineering Aspects*, vol. 377, no. 1, pp. 297–303, 2011.

[74] M. Chen, J. Parot, V. A. Hackley, S. Zou, and L. J. Johnston, "Afm characterization of cellulose nanocrystal height and width using internal calibration standards," *Cellulose*, vol. 28, no. 4, pp. 1933–1946, 2021.

[75] H. H. Winter and F. Chambon, "Analysis of linear viscoelasticity of a crosslinking polymer at the gel point," *Journal of Rheology*, vol. 30, p. 367, 2 1986.

[76] E. E. Ureña-Benavides, G. Ao, V. A. Davis, and C. L. Kitchens, "Rheology and phase behavior of lyotropic cellulose nanocrystal suspensions," *Macromolecules*, vol. 44, no. 22, pp. 8990–8998, 2011.

[77] S. Onogi and T. Asada, "Rheology: Volume 1: Principles," in Springer US, 1980, ch. Rheology and Rheo-Optics of Polymer Liquid Crystals.

[78] W. J. Orts, L. Godbout, R. H. Marchessault, and J. .-. Revol, "Enhanced ordering of liquid crystalline suspensions of cellulose microfibrils: A small angle neutron scattering study," *Macromolecules*, vol. 31, no. 17, pp. 5117–5725, 1998.

[79] S. Shafiei-Sabet, W. Y. Hamad, and S. G. Hatzikiriakos, "Rheology of nanocrystalline cellulose aqueous suspensions," *Langmuir*, vol. 28, no. 49, pp. 17 124–17 133, 2012.

[80] S. Shafeiei-Sabet, W. Y. Hamad, and S. G. Hatzikiriakos, "Influence of degree of sulfation on the rheology of cellulose nanocrystal suspensions," *Rheologica Acta*, vol. 52, no. 8, pp. 741–751, 2013.

[81] A. D. Haywood, K. M. Weigandt, P. Saha, M. Noor, M. J. Green, and V. A. Davis, "New insights into the flow and microstructural relaxation behavior of biphasic cellulose nanocrystal dispersions from rheosans," *Soft Matter*, vol. 13, pp. 8451–8462, 45 2017.